



Mechanism, *ab initio* calculations and microkinetics of hydrogenation, hydrodeoxygenation, double bond migration and *cis-trans* isomerisation during hydrotreatment of C₆ secondary alcohol species and ketones

Brigita Hočvar, Miha Grilc*, Matej Huš, Blaž Likozar

Department of Catalysis and Chemical Reaction Engineering, National Institute of Chemistry, Hajdrihova 19, 1000 Ljubljana, Slovenia



ARTICLE INFO

Article history:

Received 17 February 2017

Received in revised form 4 June 2017

Accepted 17 June 2017

Available online 19 June 2017

Keywords:

Oxygenate model compounds

Hexanol and hexanone

Hydrogenolysis

Reaction kinetics modelling

DFT mechanism

ABSTRACT

Hydrotreatment of secondary hexanone and hexanol, and primary hexene species was investigated over the sulphide-form NiMo/γ-Al₂O₃ heterogeneous catalyst within the process temperature range 200–275 °C. The mechanistic microkinetic model for a three-phase slurry reactor was developed, comprising the mass transfer flux from the dispersed gaseous H₂ bubbles to liquid solvent bulk, the external convective resistance at catalytic surface interface, material lattice adsorption and desorption, and intrinsic conversion kinetics (homogeneous and catalysed). It reported the reaction rate constants and activation energies for ketones and alcohols. Intermediate alkene isomers were identified and quantified, demonstrating the same reactive selectivity regardless of the cascade reactant compound. Furthermore, the C₆ olefin isomerisation studies under pressurised hydrogen and nitrogen (up to 9.5 times slower) atmospheres indicated a similar equilibrium distribution of the concentrations of 1-hexene, *cis*-2-hexene, *trans*-2-hexene, *cis*-3-hexene and *trans*-3-hexene. The position of the oxygen-containing (heteroatom) functional group on an aliphatic hydrocarbon chain exhibited only a minor kinetic effect on parallel and serial hydrogenation or de-hydroxylation steps. Quantum chemical (QC) calculations utilising density functional theory (DFT) computational framework were performed to elucidate the mechanism of hydrodeoxygenation (HDO). The competing main and side pathways were considered in calculating transition state barriers. Simulations showed a very good agreement with measured experimental data. Deoxygenation valorisation routes were examined as they are vital upon converting ligno-cellulosic biomass resources and for the production of the bio-based platform oxygenates in bio-refineries. Hexose(s), for example, are (poly)alcohols, the monomer building blocks of cellulose, which is besides lignin and hemicellulose the principal wood, grass and straw constituent.

© 2017 Elsevier B.V. All rights reserved.

1. Introduction

Fossil fuels are still the main energy source for transportation fuels and the primary source of chemicals despite an increasing use of renewable feedstock. Lignocellulosic biomass conversion processes have attracted significant interest to produce not only biofuels but also promising platform chemicals. Lignocellulosic biomass is composed of cellulose (40–50%), hemicellulose (25–35 %) and lignin (15–20 %). The conversion of latter is currently a topic of wide scientific research efforts. Cellulose is an especially promising component because it contains a single monomeric unit

(glucose), offering high yields and selectivity upon conversion into platform chemicals [1–5].

In contrast to fossil fuels, biomass contains a high amount of oxygen-containing functional groups, present in both aromatic and aliphatic structures. Cellulose- and hemicellulose-derived sugars contain even more oxygen than lignin monomers, often necessitating various catalytic steps (including dehydration, dehydrogenation, hydrogenolysis, hydrogenation, aldol-condensation, *trans*-esterification, isomerisation and hydrodeoxygenation) for conversion into platform and added-value chemicals. Hydrodeoxygenation (HDO) has been identified as an important step in upgrading oxygen-containing biomass compounds into fuels or added value chemicals [6–8].

Understanding the HDO mechanism of each individual functional group is crucial in understanding reaction pathways and

* Corresponding author.

E-mail address: miha.grilc@ki.si (M. Grilc).

kinetics of more complex compounds or their mixtures (e.g. pyrolysis oil). Thus, it is fundamental for kinetic modelling on either molecular or lumped basis. Furimsky [8] summarized the mechanisms, apparent kinetic rate constants and activation energies for HDO of oxygen-containing groups in biomass-derived feedstocks. The HDO reaction requires relatively high hydrogen pressure (5–20 MPa) and temperature (100–300 °C) in the presence of a heterogeneous catalyst [9,10].

Many authors investigated HDO of individual aliphatic ketone and alcohol functional groups [8–12] from eventual biomass-derived compounds in aqueous or nonpolar media or in a gaseous phase with various homogenous or heterogeneous catalysts. In comparison to nonpolar solvents, water could be a disruptive factor for HDO due to its competitive adsorption on the active sites and its eventual influence on dehydration step (reverse reaction) [12]. Similar observations were reported by Peng et al. who studied kinetics and reaction pathways for HDO of C₃ alcohols in a gaseous and liquid phase over Pt catalyst on aqueous alumina support. Due to destruction of aluminium oxide in aqueous medium, the rate of dehydration is two orders of magnitude faster in gaseous phase. Additionally, decarbonylation was also observed [13].

The use of a relatively inexpensive catalyst that is stable and active at the desired reaction conditions is crucial for successful HDO. Sulphided transition-metal catalysts, such as MoS₂, promoted by Co or Ni on Al₂O₃ support, are known to be active and are therefore widely used for HDO reactions in nonpolar solvents [14]. Senol [15,16] investigated the HDO of aromatic and aliphatic oxygenates over conventional sulphided NiMo and CoMo catalysts on Al₂O₃ support, which are most extensively tested for HDO reactions on the laboratory scale and used commercially for hydrodesulphurization (HDS). Mo represents an active metal element, while Ni and Co serve as promoters, whereas the vacancies, located on the edges of MoS₂ nanoclusters, are the active sites of the acidic character, which create strong interaction with the alumina support. It is well known that γ-Al₂O₃ support has a great potential due to its high surface area and excellent crushing strengths [17].

Heterogeneous catalytic reactions have been widely studied, also by including kinetic modelling. Most research, however, uses traditional well-known kinetic models, such as adsorption reaction model Langmuir–Hinshelwood, Eley–Rideal models and other simplified kinetic models [3,18,19]. The microkinetic modelling has been a challenge for a multiphase reaction process, because it demands a fundamental understanding of the reaction mechanism on a molecular level. Elementary steps in catalytic reactions, and interaction of substrates, intermediates and products with active sites on the catalyst surface must be well described. Guo et al. [20] reviewed challenges in modelling and the progress in metal-catalysed biomass conversions, such as hydrogenation and hydrodeoxygenation of biomass derived compounds.

In this work, HDO of linear C₆ ketones and secondary C₆ alcohols over NiMo/γ-Al₂O₃ was investigated to glean a comprehensive understanding of the reaction routes in HDO of the ketones and secondary alcohols. All plausible dehydration, dehydrogenation, hydrogenation, C–C and C–O scission routes have been investigated in great detail to propose a reaction pathway network. Beside liquid and gaseous phase analysis, hydrogen consumption was calculated using the Peng–Robinson equation of state (EOS) from measured temperature, pressure, known volume and gas composition. It was compared to consumption according to the formation of intermediates and products in the liquid phase. Moreover, ketone and alcohol HDO and isomerisation of hexenes (including *cis*- and *trans*-) were studied in detail.

Based on experimental data, a microkinetic mathematical model for a batch three-phase process was developed, explicitly accounting for mass transfer phenomena, adsorption and desorption kinetics and elementary reaction steps on the catalyst surface. The

mathematical model values were fitted to experimental data in order to obtain the corresponding parameters. *Ab initio* quantum chemical calculations were performed to complement experimental data. Density functional theory (DFT) calculations were used to calculate the activation energies and equilibrium constants for comparison with calculated values from modelling and in turn for explanation of reaction mechanisms, which were compared with their values from microkinetic modelling, showing remarkable agreement.

2. Experimental

2.1. Catalyst characterisation

A commercially available bifunctional NiMo/γ-Al₂O₃, which was sulphided off-site in the laboratory Totsucat process Eurecat (La Voulte-sur-Rhône, France) by the H₂S/H₂ sulphiding agent, was used in all catalytic experiments and it was characterized before use. Milled sulphided bifunctional catalyst with diameter under 100 μm was structurally characterized by the field emission scanning electron microscopy (FEG-SEM), energy dispersive X-ray spectroscopy (EDX) and the X-ray powder diffraction (XRD) analysis. The specific surface area (A_{BET}) was determined by the Braunauer–Emmett–Teller method (BET) using ASAP 2020 instrument for N₂-physisorption. Concentration of active sites on the catalyst was measured using Micrometrics AutoChem II Chemisorption Analyzer (Micrometrics, Norcross, GA, USA) with the TPR-TPO-TPR method [21]. Detailed description of the characterization methods and some additional characterization results for the same catalyst are reported in our previous works [22,23].

2.2. Hydrodeoxygenation process

Catalytic HDO experiments were performed in a cylindrical 300 mL batch stainless steel autoclave (Parker Autoclave Engineers) with the inner diameter of 43 mm and the height of 210 mm, equipped with a magnetically driven Rushton turbine impeller, located 25 mm above the reactor bottom, with the diameter of 30 mm. The reactor was filled with 120 mL of reaction mixture, containing 90 wt% of dodecane (≥99 wt%, Sigma-Aldrich) solvent and 10 wt% of a model compound. Catalytic experiments included 25 wt% of the catalyst with respect to the mass of model compound. Model compounds used for experiments were 2-hexanone (≥99 wt%, Sigma-Aldrich), 3-hexanone (≥98 wt%, Sigma-Aldrich), 2-hexanol (≥99 wt%, Sigma-Aldrich), 3-hexanol (≥97 wt%, Sigma-Aldrich) and 1-hexene (≥99 wt%, Sigma-Aldrich). Conventional sulphided NiMo/γ-Al₂O₃ catalyst was ground and sieved to obtain particles with diameters smaller than 100 μm. Reactor was attached to the housing, sealed and had a heating belt mounted. The whole system was flushed with nitrogen (5.0, Messer, Bad Soden am Taunus, Germany) and then filled with hydrogen (5.0, Messer, Bad Soden am Taunus, Germany) to the desired pressure. Experiments were performed in a batch regime. Agitation speed was kept constant at 16.7 s⁻¹ to ensure complete dispersion of the catalyst particles and gaseous phase aspiration. All experiments initiated at room temperature, while the reactor content was heated-up at the heating rate of 7.5 K min⁻¹ to the desired temperature by an electric jacket heater, controlled by a PID regulator. After keeping the reaction mixture at the set temperature for 60 min, the reactor was rapidly cooled down, the gas phase was gradually released and the headspace of the reactor was purged with nitrogen before opening (Table 1).

Table 1

Reaction conditions for each run in slurry batch reactor, where dodecane was used as solvent and H₂ or N₂ as gas phase.

Run	Model compound	T ^a (°C)	P ^b (MPa)	w _{cat} ^c (wt%)
1	2-hexanol	225	5 ^c	25
2	2-hexanol	250	5 ^c	25
3	2-hexanol	275	5 ^c	25
4	2-hexanol	250	5 ^c	0
5	2-hexanone	225	5 ^c	25
6	2-hexanone	250	5 ^c	25
7	2-hexanone	275	5 ^c	25
8	2-hexanone	250	5 ^c	0
9	3-hexanol	225	5 ^c	25
10	3-hexanol	250	5 ^c	25
11	3-hexanol	275	5 ^c	25
12	3-hexanol	250	5 ^c	0
13	3-hexanone	225	5 ^c	25
14	3-hexanone	250	5 ^c	25
15	3-hexanone	275	5 ^c	25
16	3-hexanone	250	5 ^c	0
17	1-hexene	200	5 ^c	25
18	1-hexene	250	5 ^c	25
19	1-hexene	250	5 ^d	0
20	1-hexene	250	5 ^d	25

^a Set temperature of plateau.

^b Initial pressure in reactor.

^c Hydrogen atmosphere.

^d Nitrogen atmosphere.

^e Mass of catalyst per mass of model compound.

2.3. Reactants, intermediates and products analysis

The reactor was connected to FTIR (Fourier Transformation Infrared Spectroscopy, Spectrum 100, Perkin Elmer) and GC (Gas Chromatography) with a flame ionization detector, using helium (5.0, Messer, Bad Soden am Taunus, Germany) as a carrier gas.

Gaseous products were passed through a vertical water-cooled condenser for analysis of permanent gases, where H₂, CO, CO₂ and methane were identified and quantified. Gaseous samples were taken in approximately 25 min intervals, cooled in the condenser for 2 min, while they subsequently flushed GC sampling loop and the short path gas cell with KBr windows. Samples were scanned by Fourier transform infrared (FTIR) spectroscopy in the range of 450–4000 cm⁻¹. As samples were taken from 5 MPa pressure, their volumes at the ambient pressure were high enough to thoroughly purge the FTIR cell and GC sample loop. Before the experiment, FTIR spectrum with pure hydrogen was collected as a background. Three bands, characteristic of CO₂ absorbance, were detected at wavenumbers of 669, 2340, and 3628 cm⁻¹, of CO at 2120 cm⁻¹, and of CH₄ at 1304 and 3015 cm⁻¹. From FTIR and GC analyses, the gaseous phase composition was determined, while the amounts (moles) of the gases formed and H₂ consumed were calculated by using Peng–Robinson equations of state with van der Waals mixing rules [24].

The liquid samples were collected in 10-min intervals, filtered, diluted in heptane, and further analysed offline by Thermo Scientific gas chromatograph (Focus GC, Thermo Scientific, MA, USA), equipped with a capillary column ZB-5MS (60 m × 0.25 mm × 0.25 µm, Phenomenex, Torrance, CA, USA) and a flame ionization detector. Temperature programmed method was used for liquid samples analysis, where the oven was initially kept at 313 K for 7.2 min, then the temperature was increased to 383 K (with heating-up rate of 25 K min⁻¹), then to 498 K by 18 K min⁻¹ rate and finally to 553 K by 40 K min⁻¹ rate. It was then kept constant for 6 min, ensuring complete elution of all products from the column. The injector and detector were maintained at 568 K, the injection volume was 1 µL and the split ratio was set to 50. In order to quantify the products, the external 6-point calibration was carried out with standards purchased from Sigma–Aldrich.

Table 2

Notation, Latin letters.

Notation	Unit
a _g	m ⁻¹
a _s	m ⁻¹
AS	kmol m ⁻² (also µmol m ⁻²)
BET	m ² kg ⁻¹ (also m ² g ⁻¹)
c _{as}	kmol m ⁻³ (also mol L ⁻¹)
c _{H2}	kmol m ⁻³ (also mol L ⁻¹)
c _n	kmol m ⁻³ (also mol L ⁻¹)
d _a	m
d _b	m
d _r	m
D _{AB}	m ² s ⁻¹
Ea	J mol ⁻¹
g	m s ⁻²
ΔG	J mol ⁻¹ K ⁻¹
h	K s ⁻¹ (also K min ⁻¹)
H _a	m
H _l	m
k _g	s ⁻¹
k _l	m s ⁻¹
k _n	Depends on rate expression
K _{eq}	/
m _{cat}	kg
M _{dodecane}	kg kmol ⁻¹
N	s ⁻¹
N*	s ⁻¹
p	MPa
r _n	mol L ⁻¹ s ⁻¹
R	J mol ⁻¹
Sc	/
t	s
T	K
V	L
V _D	cm ³ mol ⁻¹
V _M	cm ³ mol ⁻¹

Table 3

Notation, Greek letters.

Notation	Unit
α	Coefficient (Eq. (5)) = 500
β	Coefficient (Eq. (8)) = 0.0449
ε_g	Gas hold up
μ_l	Dynamic viscosity
ρ_l	Density of liquid phase
ρ_g	Density of the gas phase
$\Delta\rho$	Solid – liquid density difference
σ_l	Surface tension of the liquid phase

Table 4

Superscripts.

Notation	
ads	Adsorption/adsorbed
cat	Catalytic (reaction)
des	Desorption
g	In gas phase
hom	Homogeneous (reaction)
i	On the interphase
l	In liquid phase
s	On solid phase

Table 5

Abbreviations.

Notation	
BET	Braunauer–Emmett–Teller method
DFT	Density functional theory
EDX	Energy dispersive X-ray spectroscopy
EOS	Equation of state
FEG-SEM	Field emission scanning electron microscopy
FTIR	Fourier Transformation Infrared Spectroscopy
GC	Gas Chromatography
GC-MS	Gas Chromatography – Mass spectroscopy
HDO	Hydrodeoxygenation
HDS	Hydrodesulphurization
XRD	X-ray powder diffraction

Identification of intermediates and products was confirmed as a match of mass spectra and retention indices determined by GC-MS (Ultra 2010, Shimadzu, Kyoto, Japan) and standards from NIST 14 and FFNSC 2 libraries.

3. Microkinetic model

Hydrodeoxygenation of liquid model compounds over a solid catalyst with a gaseous reactant is a three-phase reaction process, entailing mass transfer from gaseous to liquid phase (and vice-versa), from the liquid phase to the catalyst surface (and vice-versa), adsorption, desorption and chemical reaction of reactive species on the catalyst surface and, eventually, non-catalysed transformations in a bulk liquid. Based on detected intermediates and products in gaseous and liquid phase, individual process steps were proposed, and a reaction mechanism was postulated and applied in a mathematical microkinetic model. The mathematical model developed was used to determine the mass transfer, adsorption/desorption and kinetic rates and the contribution of each evaluated phenomena to the overall rate of transformation (Tables 2–5).

3.1. Transfer of hydrogen from gaseous to bulk liquid phase

Hydrogen is aspirated from the reactor headspace into the liquid phase through dispersed bubbles. Its intrinsic concentration ($C_{H_2}^i$) on the liquid side of the gas-liquid interphase was evaluated with Henry's law. The corresponding temperature-dependant Henry's constant (the value of $459.64 \cdot e^{(-0.004258 \cdot T)}$ MPa) for

operating conditions relevant for this work was proposed by Gao et al. [25].

$$C_{H_2}^i = \frac{p_{H_2}^g \cdot \rho_l M_{\text{dodecane}} \cdot 459.64 \cdot e^{(-0.004258 \cdot T)}}{(1)$$

Relations for evaluating the parameters describing the transfer of the hydrogen from gaseous to liquid phase were taken from the literature, including characteristic stirrer speed (N^*) [26]:

$$N^* = \sqrt[4]{\frac{\sigma_l \cdot g}{\rho_l}} \cdot \frac{2 \cdot d_r}{d_a^2} \cdot \left(\frac{H_l - H_a}{H_l} \right)^{\frac{1}{2}} \quad (2)$$

The actual stirrer speed was greater than the characteristic stirrer speed ($N \geq 2N^*$), making the gas bubbles diameter and gas–liquid mass transfer coefficient independent of the agitation speed [8], instead being influenced only by the density difference between the two phases, and the surface tension of the liquid [27]:

$$d_b = \left(\frac{0.41 \cdot \sigma_l}{g \cdot (\rho_l - \rho_g)} \right)^{\frac{1}{2}} \quad (3)$$

$$\sigma_l = (54.825 - 0.913 \cdot T) \times 10^{-3} \quad (4)$$

When average gas bubble diameter is smaller than 2×10^{-3} m, the gas–liquid transfer coefficient can be calculated from the equation by Van Dierendonc [26]:

$$k_g = 0.42 \cdot \left(\frac{\mu_l \cdot g}{\rho_l} \right)^{\frac{1}{3}} \cdot Sc^{-\frac{1}{2}} \cdot \alpha \cdot d_b \quad (5)$$

where α is 500 m^{-1} . Dynamic viscosity (μ_l) of the reaction mixture is temperature-dependent and calculated from Andrade's equation [28]:

$$\ln(\mu_l) = A + \frac{B}{T} \quad (6)$$

where A and B are the characteristic parameters obtained by regression analysis of experimental data, valued -4.545 and 1445, respectively, to that give the viscosity in mPas units. Dynamic viscosity was used to calculate the Schmidt number (Sc):

$$Sc = \frac{\mu_l}{\rho_l \cdot D_{AB}} \quad (7)$$

Diffusion coefficient (D_{AB}) was calculated from a correlation, reported by Matthews et al. [29]:

$$\frac{D_{AB}}{T^{\frac{1}{2}}} = \beta \cdot (V_M - V_D) \quad (8)$$

where the parameters β and V_D (molar volume of a solvent at which diffusion goes to zero) for hydrogen in dodecane are 0.0449 and 218 ($\text{cm}^{-3} \text{ mol}^{-1}$ units should be used), respectively. Molar volume of solvent (V_M) was calculated from molar mass and density of the solvent. Gas hold-up fraction in the liquid phase was calculated from the equation, proposed by Froment and Bishoff for a closed reactor system [26], assuming that the agitation speed is greater than the characteristic stirrer speed (N^*), which is in our case 7.0 s^{-1} . The stirring speed used in our experiments (N) was set to 16.7 s^{-1} .

$$\varepsilon_g = 0.45 \frac{(N - N^*) \cdot d_a^2}{d_r \cdot \sqrt{g \cdot d_r}} \quad (9)$$

The interface area between the gaseous and liquid phase, defined as the ratio between the surface of the dispersed gas bubbles and the volume of the liquid phase, was calculated as:

$$a_g = \frac{6 \cdot \varepsilon_g}{d_b} \quad (10)$$

3.2. Mass transfer from liquid phase to catalyst surface

Hydrogen and a model compound are transferred from the liquid phase to the external surface of catalyst particles. The liquid-solid mass transfer coefficient for a small sphere particle falling freely at its terminal velocity is calculated from the equation by Satterfield and Sherwood [30].

$$k_l = 0.34 \cdot \left(\frac{\Delta\rho \cdot \mu_l \cdot g}{\rho_l^2} \right)^{\frac{1}{3}} \cdot (Sc)^{-\frac{2}{3}} \quad (11)$$

where $\Delta\rho$ is density difference between the solid and liquid phase. Density of the solid phase ($\text{NiMo}/\gamma\text{-Al}_2\text{O}_3$) particles was set to 2 g cm^{-3} , density of liquid phase was considered temperature-dependent as defined by Lemmon et al. [31]. Diffusion coefficients of hydrogen and model compounds in dodecane have been evaluated from the equations by Matthews et al. [29].

Liquid-solid interfacial area was based on catalyst characterization and can be calculated as product of the specific area, defined by BET method, and mass of the added catalyst (Eq. (12)):

$$a_s = \frac{\text{BET} \cdot m_{\text{cat}}}{V_l} \quad (12)$$

3.3. Adsorption and desorption kinetics

Kinetic rates of adsorption and desorption were defined as follows:

$$r_n^{\text{ads}} = k_n^{\text{ads}} \cdot c_n^s \cdot c_{\text{as}} \quad (13)$$

$$r_n^{\text{des}} = k_n^{\text{des}} \cdot c_n^{\text{ads}} \quad (14)$$

where molecular H_2 was assumed to be adsorbed and to react on the catalyst surface due to uncertain quantitative determination of the rate of H_2 dissociation on the surface. The temperature dependence of adsorption and desorption rate was not considered due to relatively small variations in absolute temperature and as adsorption/desorption steps were not found to be the rate-determining step.

3.4. Ab initio calculations

Quantum chemical methods were used to obtain first-principles mechanistic information on the reactions considered. Open-source PWscf code as implemented in Quantum Expresso 5.4 program suite [32] was used to obtain electronic structures and energies. Electronic interactions were described with ultrasoft pseudopotentials with generalized gradient approximation (GGA) and Perdew–Burke–Ernzerhof (PBE) exchange potential [33]. Brillouin zone integration was performed on $(2 \times 2 \times 1)$ Monkhorst–Pack k -point mesh. Convergence testing showed that with kinetic energy cutoff of 340 eV and electron density cutoff of 2000 eV , energies are converged to within 0.05 eV . To account for poor description of van der Waals interactions by DFT, semi-empirical DFT-D2 method of Grimme was used [34,35]. Adsorption energies were calculated as

$$\Delta E_{\text{ads}} = E_{\text{adsorbed}} - E_{\text{catalyst}} - E_{\text{adsorbate}} \quad (15)$$

where E_{adsorbed} denotes total energy of bound complex of catalyst slab and adsorbate, E_{catalyst} is the energy of empty slab and $E_{\text{adsorbate}}$ is the energy of isolated molecule to be adsorbed. Zero-point energy corrections were not included as preliminary testing showed that they mostly cancel out when comparing adsorbed intermediates and transition states in question. Transition states were located with nudge elastic band method with climbing image and deemed converged when forces on atoms were less than $0.05 \text{ eV}\text{\AA}^{-1}$.

Where we were only interested in equilibria (for hexenes isomerisation), isolated molecules were treated with Gaussian

09 program suite [36] at B3LYP density functional level and 6–311+G(3df,2p) basis set, which offers a very good compromise between accuracy and calculation cost. Solvent (dodecane) was modelled implicitly with polarizable continuum model with default parameters. Thermodynamic properties were calculated from frequency analysis in harmonic oscillator approximation on fully relaxed geometries, taking zero-point energy, vibrational, translational, and rotational contributions to the partition function into account [37]. Equilibrium constants (K_{eq}) for hexane isomerisation were calculated via

$$\Delta G = -R \cdot T \cdot \ln K_{\text{eq}} \quad (16)$$

where ΔG denotes Gibbs free energy difference between the isomers, R is the universal gas constant and T temperature. Similar methodology was used to study homogenous reactions. Transition states were located with synchronous transit-guided quasi-Newton method (STQN) and confirmed with vibrational analysis to possess exactly one imaginary frequency, corresponding to the reaction path.

Based on available characterisation data, the catalyst was modelled as follows. The unit cell consisted of four Mo_2 units in the x direction and three Mo atoms in the z direction (perpendicular to the edge). The two bottom atomic layers (Mo and S) were frozen into their bulk positions, while all other atoms were allowed to fully relax. Two adjacent top Mo atoms were substituted with Ni to take Ni promotor effects into account. When modelling the sulpho-reductive conditions (for hydrogenation reactions), a sulphur atom is placed on the bridge site above the two top Mo atoms, allowing for the formation of protonic (sulphydryl) species [38].

3.5. Chemical reaction in bulk liquid and on the catalyst surface

Although the dominant chemical transformations take place on the catalyst surface, the contribution of particular non-catalysed (homogenous) reactions in bulk liquid was considered, as well. Reaction rates on the catalyst surface depend upon the surface concentrations of corresponding reactants.

$$r_i^{\text{cat}} = k_i^{\text{cat}} \cdot c_n^{\text{ads}} \quad (17)$$

$$r_i^{\text{cat}} = k_i^{\text{cat}} \cdot c_n^{\text{ads}} \cdot c_{\text{H}_2} \quad (18)$$

In Eq. (17), r_i^{cat} represents the kinetic rate and k_i^{cat} represents the kinetic rate constant for transformation i , I being their number, of the adsorbed model compound (c_n^{ads}). Where hydrogen (c_{H_2}) is required for the reaction, the rate expression from Eq. (18) was used.

Analogously, reaction rates of the homogeneous (non-catalysed) transformations in the bulk liquid depend upon the component concentrations.

$$r_i^{\text{hom}} = k_i^{\text{hom}} \cdot c_n^l \quad (19)$$

$$r_i^{\text{hom}} = k_i^{\text{hom}} \cdot c_n^l \cdot c_{\text{H}_2}^l \quad (20)$$

All reaction rate constants were considered temperature-dependent according to Arrhenius law (Eq. (21)).

$$k_i^{\text{cat}}(T(t)) = k_i^{\text{cat}}(T_{\text{final}}) \cdot \exp\left(\left(-\frac{Ea_i}{R}\right) \cdot \left(\frac{1}{T(t)} - \frac{1}{T_{\text{final}}}\right)\right) \quad (21)$$

The temperature profile corresponded to the heating regime, given by following equation, where heating rate (h) was 7.5 K min^{-1} up to the final temperature (T_{final}).

$$T(t) = T_{t=0} + h \cdot t \forall T \leq T_{\text{final}} \quad (22)$$

Surface reactions rate constants (k_i^{cat}) and activation energies (Ea_i) of each reaction were determined from a mathematical function when comparing experimental data with model results.

3.6. Molar balances

The molar balance for hydrogen in gaseous phase (Eq. (23)) and mass balances for other compound in liquid phase (Eqs. (24) and (25)), on solid surface (Eqs. (26)–(29)) and adsorbed (Eq. (30) and (31)) can be described with the following differential equations:

$$\frac{dn_{H_2}^g}{dt} = -k_{H_2}^g \cdot a_g \cdot \left(\frac{p_{H_2}}{He} - c_{H_2}^l \right) \cdot V_l \quad (23)$$

$$\frac{dc_{H_2}^l}{dt} = k_{H_2}^g \cdot a_g \cdot \left(\frac{p_{H_2}}{He} - c_{H_2}^l \right) - k_{H_2}^l \cdot a_s \cdot (c_{H_2}^l - c_{H_2}^s) - \sum r_i^{hom} \quad (24)$$

$$\frac{dc_n^l}{dt} = k_n^l \cdot a_s \cdot (c_n^l - c_n^s) \pm \sum r_i^{hom} \quad (25)$$

$$V_s \frac{dc_{H_2}^s}{dt} = k_{H_2}^l \cdot a_s \cdot (c_{H_2}^l - c_{H_2}^s) \cdot V_l - k_{H_2}^{ads} \cdot c_{H_2}^s \cdot c_{as} \cdot V_l + k_{H_2}^{des} \cdot c_{H_2}^{ads} \cdot V_l \quad (26)$$

$$V_s \frac{dc_n^s}{dt} = k_n^l \cdot a_s \cdot (c_n^l - c_n^s) \cdot V_l - k_n^{ads} \cdot c_n^s \cdot c_{as} \cdot V_l + k_n^{des} \cdot c_n^{ads} \cdot V_l \quad (27)$$

As thickness of a convective film in the proximity of catalyst particles is insignificant, its volume (and the accumulation of compounds within) is negligible ($V_s \rightarrow 0$). Thus, the component concentrations on the solid–liquid interphase can be calculated using the algebraic equations instead of differential equations (Eqs. (28) and (29)):

$$c_{H_2}^s = \frac{k_{H_2}^{des} \cdot c_{H_2}^{ads} \cdot V_l + k_{H_2}^l \cdot c_{H_2}^l \cdot a_s \cdot V_l}{k_{H_2}^l \cdot a_s \cdot V_l + k_{H_2}^{ads} \cdot c_{as} \cdot V_l} \quad (28)$$

$$c_n^s = \frac{k_n^{des} \cdot c_n^{ads} \cdot V_l + k_n^l \cdot c_n^l \cdot a_s \cdot V_l}{k_n^l \cdot a_s \cdot V_l + k_n^{ads} \cdot c_{as} \cdot V_l} \quad (29)$$

Molar balances for compounds on the catalyst surface are written as:

$$\frac{dc_{H_2}^{ads}}{dt} = k_{H_2}^{ads} \cdot c_{H_2}^s \cdot c_{as} - k_{H_2}^{des} \cdot c_{H_2}^{ads} - \sum r_i^{cat} \quad (30)$$

$$\frac{dc_n^{ads}}{dt} = k_n^{ads} \cdot c_n^s \cdot c_{as} - k_n^{des} \cdot c_n^{ads} \pm \sum r_i^{cat} \quad (31)$$

where r_i^{cat} are rate expressions, defined in Eqs. (17) and (18), and presented in the reaction scheme (Fig. 2). Initial concentrations of the intermediates and products in gaseous and liquid phase and also on the catalyst surface were set to zero, except for the initial concentrations of model compounds for the specific experiment and hydrogen in gaseous phase.

Concentration of all available active sites c_{as} on the catalyst surface was determined by the catalyst characterization (TPR-TPO-TPR and BET) and is given as the amount (moles) of active sites per square meter of the catalyst surface. Concentration of (initially) available active sites for each experiment was calculated as product of the added catalyst mass, its specific surface area and mass concentration of active sites, divided by the volume of liquid phase, as follows:

$$c_{as}(t=0) = BET \cdot m_{cat} \cdot \frac{AS}{V_l} \quad (32)$$

Proposed differential equations and initial parameters including concentrations were inserted into a mathematical model. Modelling was performed in Matlab software, where numerical differentiation formulas (backward differentiation formulas, known as Gear's method) were used to solve the set of differential equations, which represent the set of molar balances

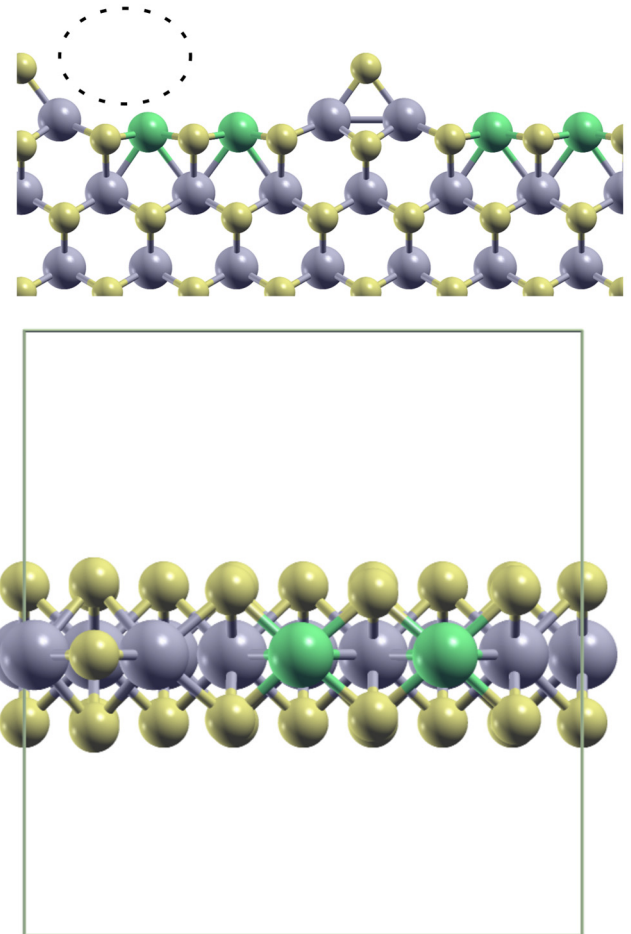


Fig. 1. Catalyst used in the DFT calculations. Top: Side-view of the catalyst, used in DFT calculations. Active site is delineated with dashed line. Bottom: Top view of active edge and cell boundaries. Colour code: beige – S, grey – Mo, green – Ni. (For interpretation of the references to colour in this figure legend, the reader is referred to the web version of this article.)

for every compound in each phase. Least-squares approximation method was employed by using Nelder–Mead simplex and Levenberg–Marquardt algorithms to determine the relevant kinetic parameters that correspond to the minimum of the objective function given by Eq. (33).

$$f(k_{1 \rightarrow 1}^{cat}, Ea_{1 \rightarrow 1}, k_{hom1 \rightarrow 1}, Ea_{hom1 \rightarrow 1}, k_{ads}, k_{des}, k_{hom}) = \sum_{exp=1}^{EXP} \sum_{i=1}^I (c_{i,j}^{meas} - c_{i,j}^{calc}(k_i^{cat}, Ea_i, k_{hom_{1 \rightarrow 1}}, Ea_{hom1 \rightarrow 1}, k_{ads}, k_{des}))^2 \quad (33)$$

Measured concentrations ($c_{i,j}^{meas}$) were simultaneously fitted to model values ($c_{i,j}^{calc}$) for all experiments (exp), EXP being their number, to obtain kinetic parameters for the hydrodeoxygenation of linear C₆ ketones and secondary C₆ alcohols.

DFT calculations were also employed to calculate activation energies of reactions on the catalyst surface and compared with energy barriers determined by the regression analysis (*vide infra*).

4. Results and discussion

4.1. Catalyst characteristics

Properties of sulphided NiMo/ γ -Al₂O₃ in terms of morphology, metal loading and surface concentration of active sites were thor-

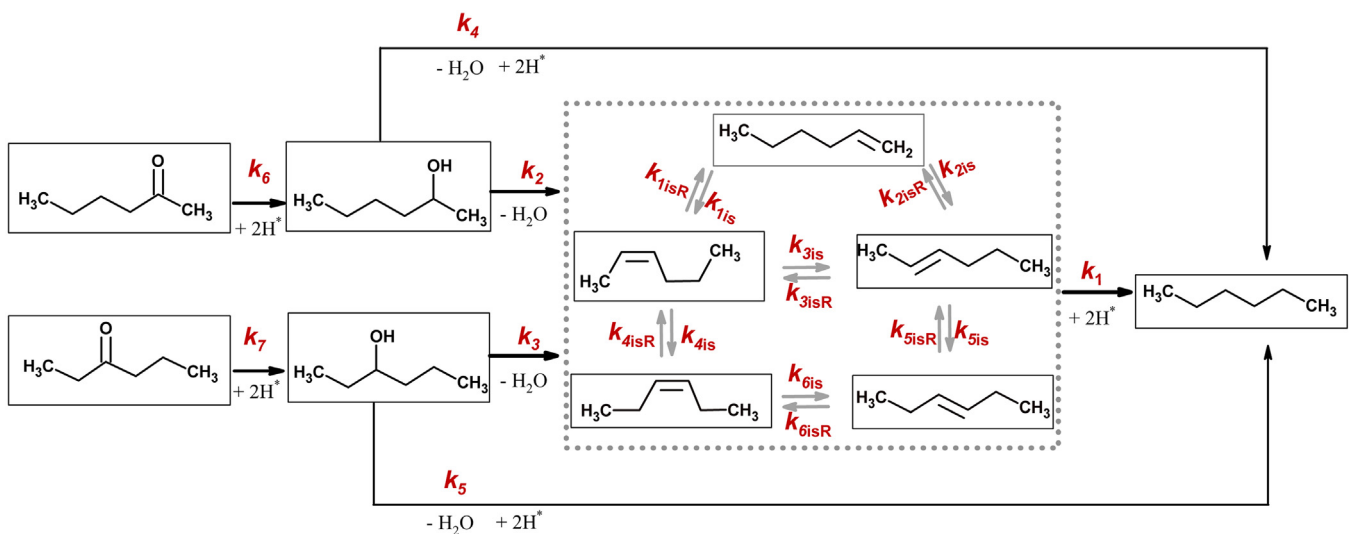


Fig. 2. Proposed reaction scheme for hydrotreatment of model compounds: 2-hexanone, 2-hexanol, 3-hexanone and 3-hexanol over NiMo/γ-Al₂O₃ catalyst.

Table 6

NiMo/Al₂O₃ catalyst characterisation results after the sulphidation.

Catalyst	Metal content (wt.%)	Active Phase	AS-Active sites ($\mu\text{mol m}^{-2}$)	BET-Surface Area ($\text{m}^2 \text{g}^{-1}$)	Pore volume ^a ($\text{cm}^3 \text{g}^{-1}$)	Pore size ^b (nm)
NiMo/Al ₂ O ₃	3/15 ^c	NiMoS _x	0.33 ^d	170	0.471	8.9

^a Total pore volume at relative pressure of 0.97.

^b Average pore diameter determined from the N₂ desorption branch by using BJH method.

^c As mass content of NiO and MoO₃ respectively for fresh catalyst.

^d Determined according NiMoO₄ surface concentration.

oughly discussed in our previous works [22,23]. Relevant catalyst characteristics are summarized in Table 6. The concentration of active sites was determined to be 0.33 $\mu\text{mol m}^{-2}$, as this value corresponds to the concentration of a main precursor for formation of HDO-active phases during the sulphidation, specifically the intimately associated fine dispersions of Ni and Mo oxides or their hydrated solid solutions, and particularly α -NiMoO₄, β -NiMoO₄ and NiMoO₄ phases. High specific surface area and pore size reveal a well-developed and mesoporous nature of γ -Al₂O₃ support.

From the catalyst characterization one can derive that the active site has a Ni-doped MoS₂ form. As shown by DFT calculations, hydrogen dissociatively binds to Ni and S atoms, while OH and C₆ species show the affinity for the Mo site (Fig. 1). As HDO reactions are expected to proceed mainly on the catalyst edge and other exposed surfaces, sulphided NiMo/γ-Al₂O₃ was modelled as the M-edge of (Ni-doped) MoS₂ [39,40] for *ab initio* calculation purposes. The active site for reactions is the Mo-S-Mo/Ni interface as shown in Fig. 1. Hydrogen atoms bind to Ni (as hydridic species) and S (as protonic species), while oxygen (in OH) and carbon (in C₆ substrates) bind to the Mo atom. For deoxygenation reactions, the reactive site must not include the sulphur bridge, i.e. we deal with a vacancy site.

4.2. Reaction pathway network

With regard to the identified intermediates and products, obtained by experiments presented in Table 1, a reaction scheme for the catalytic hydrotreatment process was proposed. As presented in Fig. 2, similar reaction pathways are assumed for ketone and hydroxyl groups on C₂ or C₃ positions. Both, 2-hexanone or 3-hexanone were initially hydrogenated to their respective alcohols, while the -OH group was removed in subsequent (HDO) step. In GC-MS analysis, only alcohols and olefins were detected as intermediates. Based on literature and DFT calculations, dehy-

dration of alcohols is a two-step process. Initially, the C—O bond is cleaved at the Mo vacancy site, followed by the hydrogen abstraction from the adjacent carbon atom to form an olefin. Different isomers of hexene were detected, such as *cis*-2-hexene, *trans*-2-hexene, *trans*-3-hexene, *cis*-3-hexene, which is in accordance to the literature [41]. As 1-hexene was only detected in trace amounts, it was assumed to form in isomerisation of 2-hexene. All hexenes were ultimately hydrogenated into hexane, which is the sole final product of alcohols and ketones hydrotreatment. Direct hydrogenation of hexanol into hexane with a substitution mechanism was also considered, although its contribution to the overall reaction rate had previously been reported to be negligible [42]. Although all experiments were performed in a non-polar medium, phase separation of water was not observed, probably due to low volume, in contrast to the report of Palla et al. who investigated octanol hydrodeoxygenation [43]. In general, the proposed reaction scheme, from ketone, through alcohol and hexenes into hexane as final product, is in accordance with numerous previous researches on HDO of ketones and alcohols [42,44,45].

4.3. Homogeneous hydrotreatment reactions

Non-catalysed hydrotreatment runs were carried out with alcohols and ketones to evaluate the contribution of homogeneous reactions. As expected, negligible conversion of any ketone or alcohol was observed.

To the best of our knowledge, there is no systematic literature data for homogenous HDO reactions of C₆ ketones and unbranched C₆ alcohols. DFT calculations were therefore used to elucidate the probability of homogenous reactions. For homogenous hydrogenation of 2-hexanone to 2-hexanol, activation energy was calculated to be 287 kJ mol^{-1} . Activation energies for concerted dehydration of 2-hexanol to *trans*-2-hexene is 245 kJ mol^{-1} . Such high barriers make these reactions kinetically inaccessible even at high

temperature and hydrogen pressure. It is well known that homogeneous dehydration of simple alcohols proceeds much more readily after protonation of alcohols [46], which converts hydroxyl group into a good leaving group ($\text{R}-\text{H}_2\text{O}^+$). However, since there is no source of acidic protons in our experimental set-up, the aforementioned homogenous reactions can be ruled out. Calculated activation energy for homogenous hydrogenation of 1-hexene to hexane is 260 kJ mol^{-1} . The aforementioned reactions did not occur during the experiment, making calculation results congruent with experimental data.

On the other hand, homogeneous hydrogenation of 1-hexene was experimentally observed (Fig. 5). Not only were non-negligible amounts of hexane formed, *trans*-2-hexene, *cis*-2-hexene, *trans*-3-hexene and *cis*-3-hexene were also observed upon carrying out the reaction without the catalyst in hydrogen atmosphere. With neither the catalyst nor hydrogen present (inert nitrogen atmosphere was used), however, these reactions did not take place. DFT-calculated activation barrier for isomerisation of 1-hexane to *trans*-2-hexane was 339 kJ mol^{-1} , making the reaction highly improbable. When molecular H_2 participates in the isomerisation reaction, the energy of the transition state is lowered to 204 kJ mol^{-1} , making this reaction possible at elevated temperatures and hydrogen pressures consistent with our experimental data (Table 7).

Gas phase analysis revealed no CO , CO_2 or CH_4 formation, which also confirmed that homogeneous reactions of decarbonylation, decarboxylation or methanation were negligible.

Table 7

Homogeneous hydrogenation and isomerisation rate constants determined by the regression analysis.

i	$k_{i(T=250^\circ\text{C})}^{\text{hom}}$	r_i^{hom}
$1_{1\text{en}->\text{hexan}}$	$1.4 \times 10^{-2} \text{ L mol}^{-1} \text{ min}^{-1}$	$k_i c_{1\text{en}}^{\text{hom}} c_{\text{H}_2}^{\text{hom}}$
$1_{c-2\text{en}->\text{hexan}}$	$9.4 \times 10^{-3} \text{ L mol}^{-1} \text{ min}^{-1}$	$k_i c_{c-2\text{en}}^{\text{hom}} c_{\text{H}_2}^{\text{hom}}$
$1_{t-2\text{en}->\text{hexan}}$	$9.8 \times 10^{-3} \text{ L mol}^{-1} \text{ min}^{-1}$	$k_i c_{t-2\text{en}}^{\text{hom}} c_{\text{H}_2}^{\text{hom}}$
$1_{t-3\text{en}->\text{hexan}}$	$1.1 \times 10^{-2} \text{ L mol}^{-1} \text{ min}^{-1}$	$k_i c_{t-3\text{en}}^{\text{hom}} c_{\text{H}_2}^{\text{hom}}$
$1_{c-3\text{en}->\text{hexan}}$	$1.2 \times 10^{-2} \text{ L mol}^{-1} \text{ min}^{-1}$	$k_i c_{c-3\text{en}}^{\text{hom}} c_{\text{H}_2}^{\text{hom}}$
1is	$1.5 \times 10^{-2} \text{ min}^{-1}$	$k_i c_{1\text{en}}^{\text{hom}}$
2is	$1.8 \times 10^{-2} \text{ min}^{-1}$	$k_i c_{1\text{en}}^{\text{hom}}$
3is	$9.2 \times 10^{-3} \text{ min}^{-1}$	$k_i c_{c-2\text{en}}^{\text{hom}}$
4is	$2.1 \times 10^{-2} \text{ min}^{-1}$	$k_i c_{c-2\text{en}}^{\text{hom}}$
5is	$2.7 \times 10^{-2} \text{ min}^{-1}$	$k_i c_{t-2\text{en}}^{\text{hom}}$
6is	$2.6 \times 10^{-4} \text{ min}^{-1}$	$k_i c_{t-3\text{en}}^{\text{hom}}$
6	$1.6 \times 10^{-4} \text{ L mol}^{-1} \text{ min}^{-1}$	$k_i c_{c-3\text{en}}^{\text{hom}}$
7	$1.2 \times 10^{-3} \text{ L mol}^{-1} \text{ min}^{-1}$	$k_i c_{3\text{on}}^{\text{hom}} c_{\text{H}_2}^{\text{hom}}$

4.4. Catalytic hydrotreatment reactions

HDO reaction pathway is presented in Fig. 2, while Figs. 4 and 5 show the experimental and calculated concentration profiles of the reactants, intermediates, and final product as a function of the reaction time.

4.4.1. Hydrotreatment of secondary C₆ alcohols

Experimental results exhibit fast conversion of both hexanols. Conversion of secondary alcohol started even before the final tem-

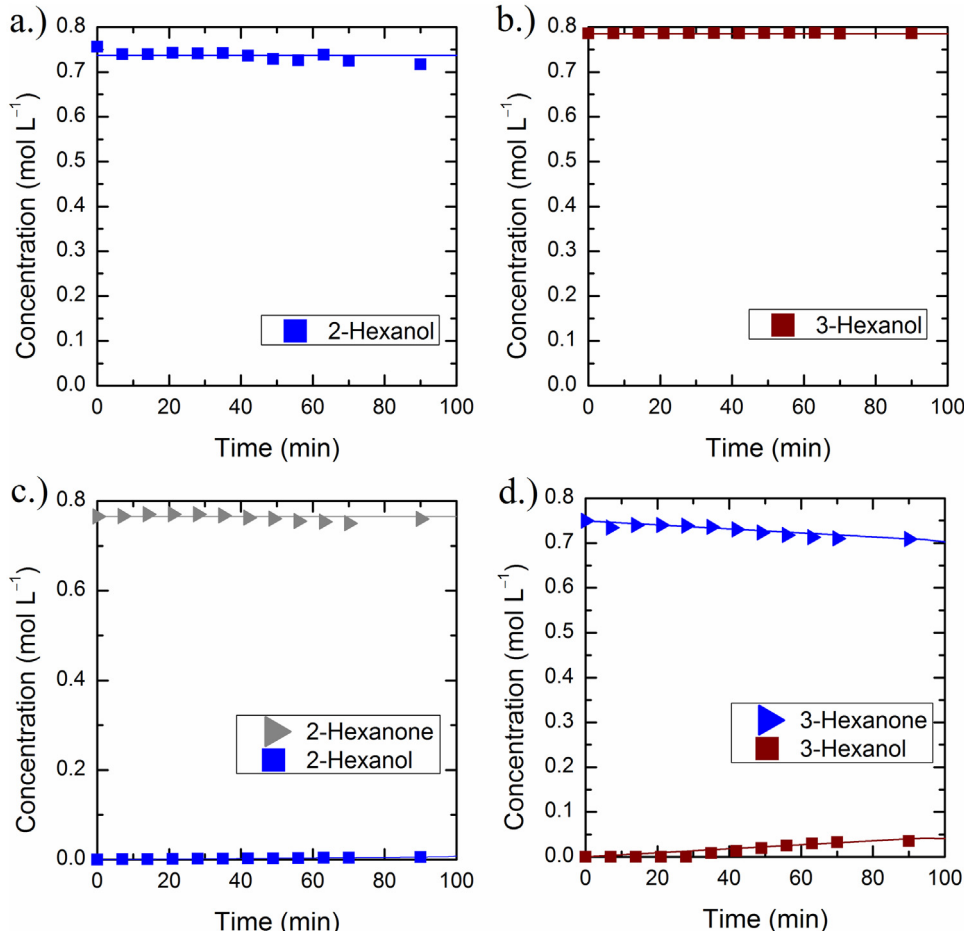


Fig. 3. Experimental data (symbols) and modelling results (lines) for non-catalysed runs. Homogeneous reactions were carried out without catalyst, at 5 MPa of hydrogen pressure and temperature 250°C , as model compounds were used: a) 2-hexanol, b) 3-hexanol, c) 2-hexanone and d) 3-hexanone.

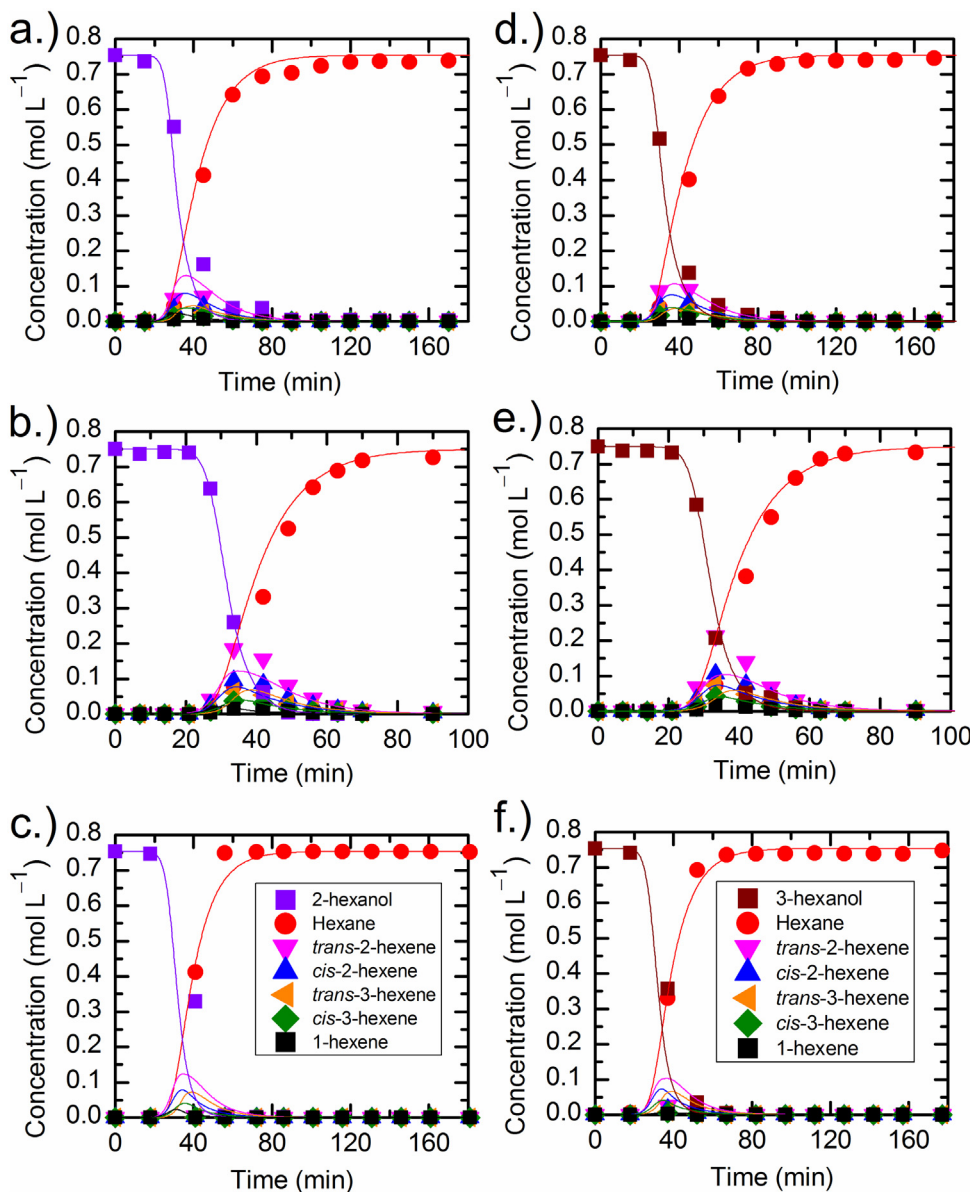


Fig. 4. Experimental data (symbols) and modelling results (lines) for hydrodeoxygenation of secondary hexanols over NiMo/γ-Al₂O₃: a.) 2-hexanol at 225 °C, b.) 2-hexanol at 250 °C, c.) 2-hexanol at 275 °C, d.) 3-hexanol at 225 °C, e.) 3-hexanol at 250 °C, f.) 3-hexanol at 275 °C. The remaining experimental conditions were kept the same: initial pressure of hydrogen of 5 MPa, stirring speed 16.7 s⁻¹, heat-up rate of 7.5 K min⁻¹, 10 wt% of model compound per mass of liquid phase, 25 wt% of catalyst per mass of model compound.

perature was reached. These results are in accordance with the research reported by Vilcocq et al. [12], where the transformation of 2-hexanol in aqueous media over a bifunctional catalytic system Pt/ZrO₂ + TiO₂–WO_x was investigated and complete conversion of 2-hexanol was reached in fixed-bed reactor at the 200–240 °C.

Based on modelling results, two possible reaction pathways of alcohol dehydration have to be considered. The main route is a concerted dehydration of alcohols and formation of olefins which are further hydrogenated to a saturated alkane, *i.e.* hexane in this work. The second route is a direct hydrogenolysis of C–O bond and subsequent hydrogenation, yielding the corresponding hydrocarbon directly. An interesting effect was observed at the highest temperature (275 °C), where hexenes were detected in trace amounts only (<0.05 mol L⁻¹). A similar effect was reported by Durand et al. [42], who detected olefins only at the lowest temperature of hydrotreatment (175 °C). In our case the reaction rate of transformation of alcohols into olefins is in accordance with the temperature depen-

dent Arrhenius law at 225 °C and 250 °C. However, at 275 °C it seems that direct hydrogenolysis of secondary hexanol into hexane has the dominant effect. Kinetic rate constants and activation energies for each step are shown in Table 8. In accordance with the results by Donnis et al. [47], the formation of ketones was observed in insignificant amounts. The cumulative concentration of the detected ketones was always below 0.005 mol L⁻¹, warranting the exclusion of alcohol dehydration into ketones was from the microkinetic mathematical model.

According to the model results, there is small difference between the rates of 2-hexanol and 3-hexanol dehydroxylation at 250 °C (4.73×10^7 and 3.50×10^7 mol L⁻¹ min⁻¹, respectively). Both proceed fast, while 1-hexanol HDO appears to be significantly slower as reported by Vilcocq [12]. During 1,2-hexanediol HDO, the preferred pathway was dehydration–hydrogenation of the secondary alcohol group. Activation energies for dehydroxylation of

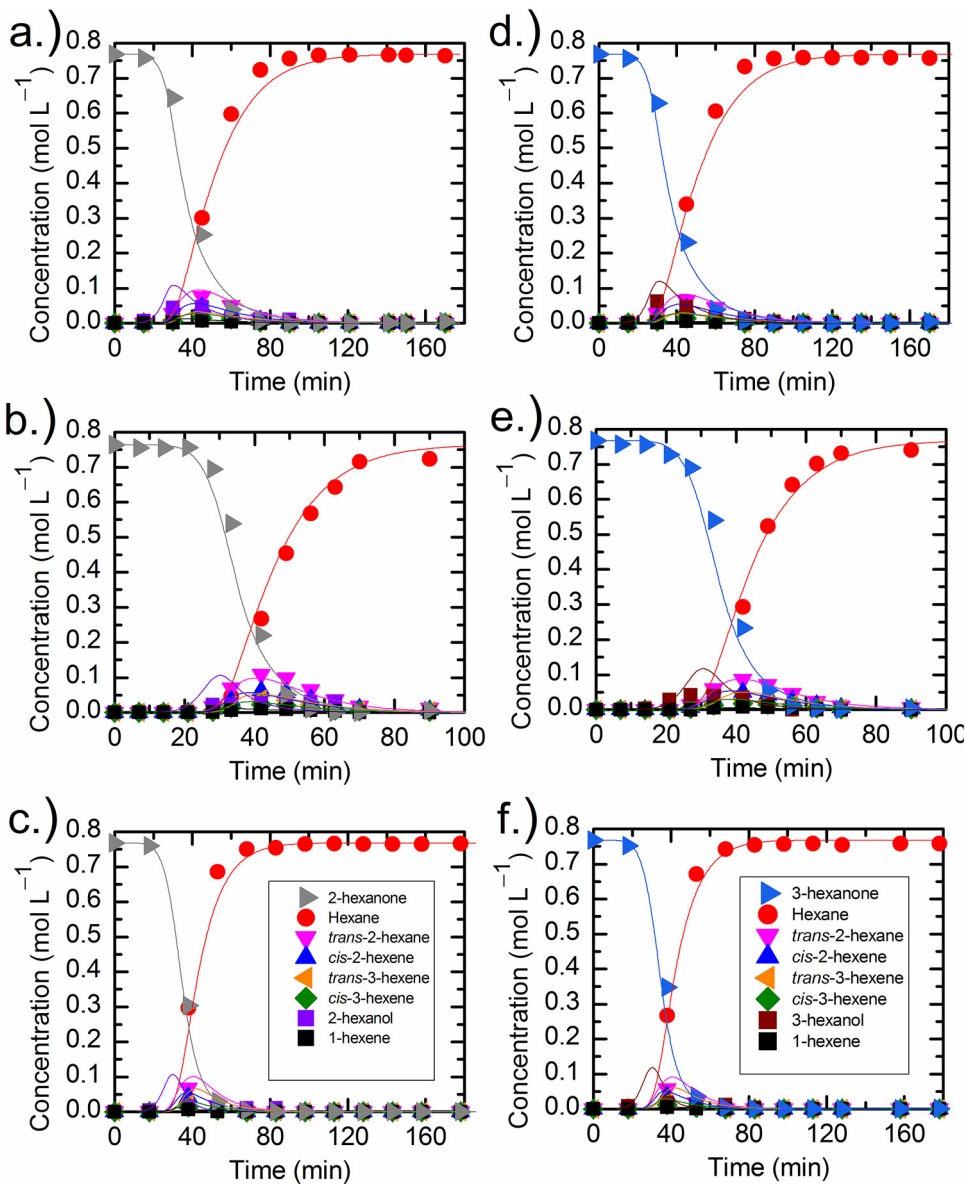


Fig. 5. Experimental data (symbols) and modelling results (lines) for hydrodeoxygenation of hexanones over NiMo/ γ -Al₂O₃: a.) 2-hexanone at 225 °C, b.) 2-hexanone at 250 °C, c.) 2-hexanone at 275 °C, d.) 3-hexanone at 225 °C, e.) 3-hexanone at 250 °C, f.) 3-hexanone at 275 °C. The remaining experimental conditions were kept the same: initial pressure of hydrogen of 5 MPa, stirring speed 16.7 s⁻¹, heat-up rate of 7.5 K min⁻¹, 10 wt% of model compound per mass of liquid phase, 25 wt% of catalyst per mass of model compound.

both secondary alcohols are quite similar; their values being 106.9 and 104.9 kJ mol⁻¹ for 2-hexanol and 3-hexanol, respectively.

For dehydration of 2-hexanol to *trans*-2-hexene over the vacancy active site, the DFT-calculated activation energy was significantly lower (65 kJ mol⁻¹). For the direct hydrogenolysis and formation of alkane, which takes place over the sulphided active site, the calculated activation energy is 134 kJ mol⁻¹ (see Section 4.6 for details).

Different hexene isomers were detected and quantified as intermediates by GC-MS; specifically, *trans*-2-hexene, *cis*-2-hexene, *trans*-3-hexene, *cis*-2-hexene and in small amounts also 1-hexene. Ryymä et al. detected various heptene isomers during 1-heptanol hydrotreatment in *n*-dodecane over sulphided NiMo/ γ -Al₂O₃ catalyst but did not quantify any of them [5]. Regardless of hydroxy group position in the alcohol used, relative abundance of hexene isomers has been consistent throughout the experiments. Their concentrations were invariably (from highest to lowest): *trans*-2-hexene, *cis*-2-hexene, *trans*-3-hexene and *cis*-3-hexene,

respectively (cf. Section 4.6 for DFT results). Final hydrogenation of hexenes into *n*-hexane resulted in 100% yield at all temperatures.

Isomerisation of hexenes was studied further. Fig. 6 shows that hydrogen is not required for hexenes isomerisation. Already at 200 °C, the isomerisation proceeded readily under nitrogen atmosphere on the catalyst surface. Catalytic isomerisation in the absence of H₂ was fast and the equilibrium was established already at 250 °C with no further change of isomer ratios. The isomerisation of olefins (1-hexene, 2-heptene and 3-heptene) in N₂ atmosphere catalysed by RhCl₃·3H₂O was discussed by Harrod and Chalk [41], who reported similar results. According to the data by Pines et al., the equilibrium ratio between *cis*-2 and *trans*-2 isomers should be 0.22, in our case this ratio between *cis*-2- and *trans*-2-hexene was 0.40 and between *cis*-3- and *trans*-3-hexene slightly higher, 0.41. As expected, isomerisation rate under nitrogen atmosphere was much slower (up to 9.5-fold) than under hydrogen atmosphere. We have completely separated hexene isomers by low-temperature separation on a 60 m long GC-MS column, while Harrod and Chalk

Table 8

Kinetic constants and activation energies for surface reactions obtained by fitting to the experimental data by Eq. 33 and from DFT calculations (cf. Fig. 8).

<i>i</i>	$k_{i(T=250\text{ }^{\circ}\text{C})}$ (min ⁻¹)	$Ea_{i,\text{exp}}$ (kJ mol ⁻¹)	r_i	$Ea_{i,\text{DFT}}$ (kJ mol ⁻¹)
1 _{1en->hexan}	8.94×10^5 ^a	10.3	$k_i c_{1en}^{ads} C_{H_2}^{ads}$	/
1 _{c-2en->hexan}	3.63×10^6 ^a	10.4	$k_i c_{c-2en}^{ads} C_{H_2}^{ads}$	/
1 _{t-2en->hexan}	1.22×10^6 ^a	9.1	$k_i c_{t-2en}^{ads} C_{H_2}^{ads}$	/
1 _{t-3en->hexan}	2.21×10^7 ^a	10.6	$k_i c_{t-3en}^{ads} C_{H_2}^{ads}$	/
1 _{c-3en->hexan}	1.39×10^6 ^a	9.8	$k_i c_{c-3en}^{ads} C_{H_2}^{ads}$	/
2	4.73×10^7	106.9	$k_i c_{2}^{ads}$	65
3	3.95×10^7	104.9	$k_i c_{3}^{ads}$	65 ^b
4	1.72×10^5 ^a	83.7	$k_i c_{20l}^{ads} C_{H_2}^{ads}$	134
5	1.50×10^6 ^a	80.4	$k_i c_{30l}^{ads} C_{H_2}^{ads}$	134 ^b
6	6.36×10^6 ^a	55.5	$k_i c_{20n}^{ads} C_{H_2}^{ads}$	45
7	6.50×10^6 ^a	55.1	$k_i c_{20n}^{ads} C_{H_2}^{ads}$	45 ^b
1is	1.76×10^4	37.1	$k_i c_{1en}^{ads}$	/
2is	1.64×10^4	27.7	$k_i c_{c-2en}^{ads}$	/
3is	3.58×10^4	21.8	$k_i c_{t-2en}^{ads}$	/
4is	3.44×10^4	21.3	$k_i c_{t-3en}^{ads}$	/
5is	1.26×10^4	44.7	$k_i c_{c-2en}^{ads}$	/
6is	0.23×10^3	41.9	$k_i c_{t-3en}^{ads}$	/

^a The unit is (L mol⁻¹ min⁻¹).

^b Assumed independent of regioisomerism.

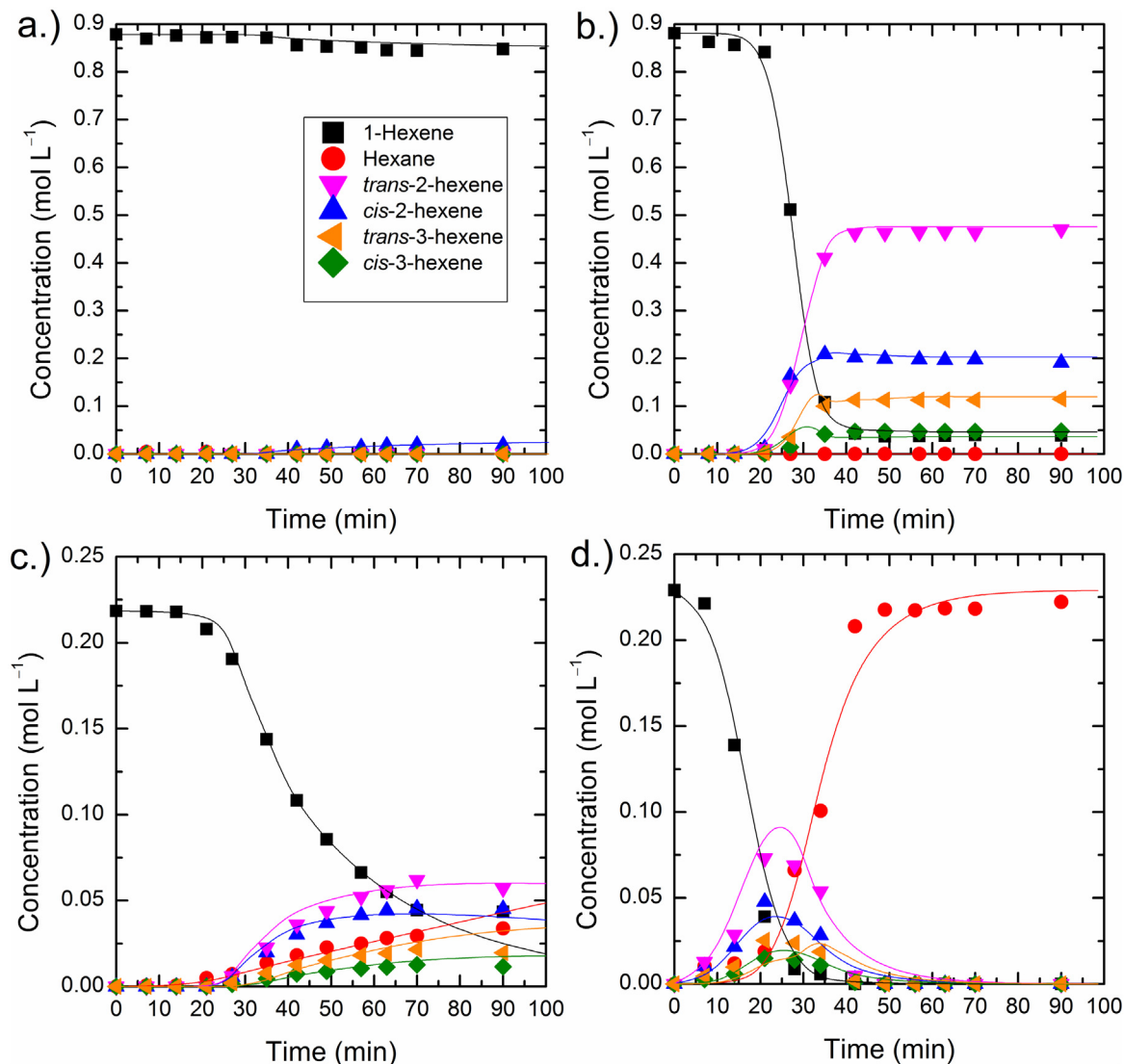


Fig. 6. Isomerisation and hydrogenation of 1-hexene, a) without catalyst in nitrogen atmosphere, at the temperature 250 °C, b) over NiMo/γ-Al₂O₃ catalyst under nitrogen atmosphere at the temperature 250 °C, c) without catalyst under 5 MPa hydrogen atmosphere at the temperature 200 °C and d) over NiMo/γ-Al₂O₃ catalyst under 5 MPa hydrogen at the temperature 250 °C.

reported convoluted peaks for 1-hexene and *trans*-3-hexene and for *cis*-3- and *trans*-2-hexene on a 6 m long oxydipropionitrile column. Under nitrogen atmosphere with NiMo/ γ -Al₂O₃ catalyst, we have definitely confirmed Harrod's hypothesis that the hydride ion required for double-bond isomerisation originates from the olefin in question, since we had no other hydrogen source. Temperature was high enough to cause catalytic C—H bond cleavage on the olefin. From experiment, isomerisation rates and equilibrium constants were determined according to the reaction scheme used. From the differences between the reaction rate of 1-hexene hydrogenation and the rate of isomerisation under nitrogen atmosphere, the rate of hydrogenation for each hexene isomer was determined by regression analysis, presented in Table 7.

To evaluate the extent of eventual decarbonylation, composition of the gaseous phase was also analysed. Negligible CO, CO₂ and CH₄ formation was observed, as shown in Fig. SD2 and Fig. SD3. This means that carbon loss during the hydrotreatment was negligible. Some formation of CH₄ could be a consequence of solvent cracking. Maximum 30 mmol of gases were formed per mol of the compound (at $t=0$). Analysis of gaseous phase after hydrotreatment of 2-hexanol and 3-hexanol showed less than 1.0×10^{-3} vol% content of CO, less than 1.2×10^{-2} vol% of CO₂ and around 0.2 vol% of CH₄ in gas phase. More than 99.7 vol% of the gas phase consisted of hydrogen. Thus, the partial pressure of hydrogen was virtually identical to the total pressure during the experiment. There was basically no difference in gas phase composition at lowest or highest reaction temperature, ruling out any temperature effect on gas formation.

Hydrogen consumption was calculated from the pressure difference in gaseous phase at known temperature, the headspace volume and gas composition. The pressure drop in the gaseous phase introduced by gas and liquid sampling was taken into account separately. Peng – Robinson equation of state combined with van der Waals mixing rule [48] was used to calculate molar composition of the gaseous phase at the corresponding temperature and pressure.

Fig. 7 shows hydrogen consumption as calculated from the pressure drop and compared to the stoichiometric amount of hydrogen required to yield the intermediates and products in the liquid phase. Senol et al. [49] reported a reduction in the total hydrogen consumption in case of dominant competitive decarbonylation and decarboxylation during aliphatic esters hydrotreatment, but did not disclose any quantitative values. As hydrogen consumption is seldom reported in a quantitative manner in the literature, quantitative calculations of hydrogen consumption, based on experimental data, are reported in this work.

Hydrogen consumption was additionally calculated according to the composition of the liquid phase. It was presumed that the presence of any hexanol in the liquid phase (in case of a hexanone feedstock) reflects in equimolar consumption of H₂, while hexane causes a double consumption of hydrogen. From the results one notices that HDO of 2-hexanol at higher temperature has a slightly higher rate of H₂ consumption.

4.4.2. Hydrotreatment of C₆ ketones

Ketone hydrotreatment was studied at the same reaction conditions. First, 2-hexanone and 3-hexanone were hydrogenated into respective alcohols. As only low concentrations of alcohols were detected in liquid samples, we can confirm that alcohol dehydration is significantly faster than its desorption or ketone hydrogenation. These results compare favourably to Vilcoq's research, who detected hexanol in trace amounts only and explained this behaviour by slower HDO of hexanone than of hexanol. However, in contrast to Vilcoq's research, who observed uncomplete conversion of 2-hexanone at 240 °C in aqueous solution over Pt catalyst, we reached a complete conversion of hexanone after 70 min at 250 °C.

Vilcoq et al. explained the uncomplete conversion with competitive adsorption of water on the catalytic sites; however their hypothesis was not backed up by a kinetic model. Hexanes were detected as intermediates in the same ratio as mentioned in the previous section. Additionally, a fast and complete hydrogenation into hexane took place. The trend in olefin concentration mirrored that from the alcohol HDO; lower concentrations were detected at higher temperatures, which is explained by greater contribution of direct alcohol transformation into alkane at higher temperatures.

According to the model values, there is no difference in activation energies for HDO of 2-hexanone and 3-hexanone, with their respective values being 55.5 and 55.1 kJ mol⁻¹. Hydrogenation of 3-hexanone in comparison to the hydrogenation of 2-hexanone was only marginally faster with model reaction rates of 6.36×10^6 and 6.50×10^6 L mol⁻¹ min⁻¹, as obtained from fitting to the experimental data.

This data is very well supported with DFT calculations, which show the rate-determining step of 2-hexanone reduction to 2-hexanol to have activation energy of 45 kJ mol⁻¹ and the overall reaction to be highly exothermic with $\Delta E = -140$ kJ mol⁻¹ (see Section 4.6 for details).

Analysis of the gaseous phase shows similar results as mentioned for HDO of 2-hexanol and 3-hexanol, i.e. negligible gas formation was observed. In HDO of ketones, higher consumption of hydrogen was observed in gaseous phase analysis, which is in agreement with mathematical calculation of the hydrogen concentration needed for HDO of ketone through alcohol into alkane. Interestingly, the opposite temperature effect was seen. At higher temperatures, H₂ consumption was slightly lower.

4.5. Transport phenomena

In Table SD1, temperature dependent mass transfer coefficients are presented. Mass transfer from gas to liquid and from liquid to the solid surface is fast enough to not be the limiting parameter. The HDO reaction is kinetically controlled, as confirmed with mathematical simulations, where the following rate relationship was discovered: Desorption > adsorption > mass transfer > kinetic reaction on the catalyst surface, where $k_H^{ads} > 10^5$ s⁻¹ and $k_{comp}^{ads} > 10^3$ s⁻¹. Adsorption and desorption rate were obtained by regression analysis and it was established that adsorption and desorption rate constant could be in persistent ratio of $k_{H_2}^{ads} = 2.5 \cdot k_{H_2}^{des}$ and $k_n^{ads} = 8.9 \cdot 10^{-2} \cdot k_n^{des}$. In that case adsorption and desorption are still fast enough not to influence the global reaction rates of transformations. As stated in the modelling section, the kinetic parameters, kinetic rates and activation energies were modelled simultaneously and are collected in Table 8. Other parameters, such as interfacial area, gas hold-up fraction, gas–liquid and liquid–solid mass transfer coefficients, were determined from correlations. As it can be seen in Table SD1, the higher the temperature, the higher the gas hold-up and, consequently, higher interfacial area between gas and liquid phase but lower gas–liquid mass-transfer coefficient. Temperature also affects the liquid–solid mass-transfer coefficients for model compounds; the higher the temperature, the higher the mass-transfer coefficient. On the other hand, temperature has lower influence on the liquid–solid mass-transfer coefficient for hydrogen. Viscosity and density of reaction mixture are also temperature-dependent; the higher the temperature, the lower the viscosity and density. Consequently, with increasing temperature a reduction of the gas bubble diameter was observed in mathematical correlations, i.e. from 0.78 mm at 225 °C to 0.58 mm at 275 °C.

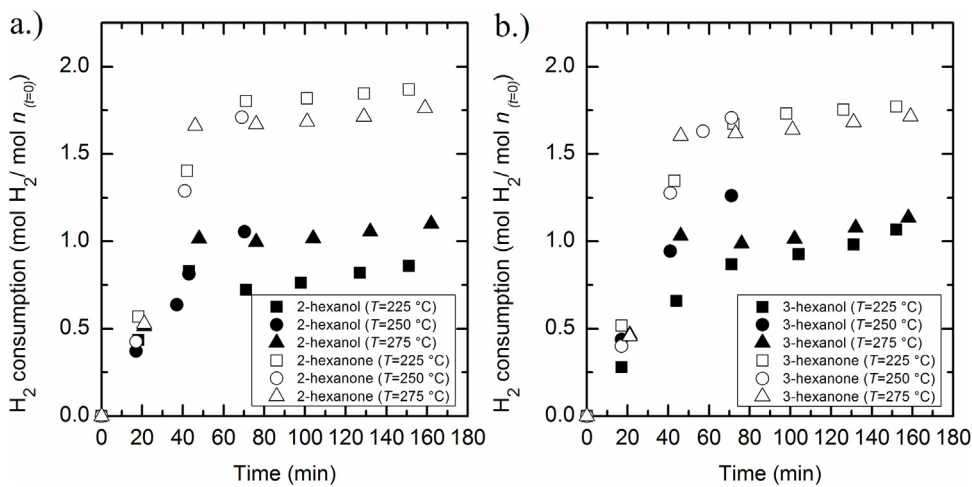


Fig. 7. Hydrogen consumption in hydrotreatment of model compounds over NiMo/γ-Al₂O₃ catalyst at different temperatures (225, 250 and 275 °C) and at the initial 5 MPa pressure of hydrogen.

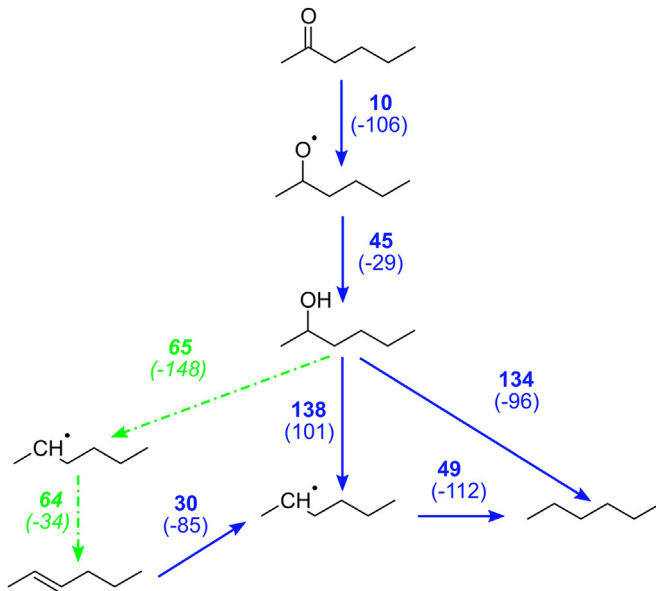


Fig. 8. Reaction network for hydrotreatment of 2-hexanone, showing all possible elementary steps. Bold numbers show activation energies, numbers in parentheses show reaction energies, all values in kJ mol⁻¹. For reasons of legibility H*, OH and H₂O are not explicitly written. Solid blue arrows represent reaction steps on the sulphided active site (favouring hydrogenation), green dot-dashed arrows with italic numbers represent reaction steps on the vacancy active site (favouring deoxygenation). (For interpretation of the references to colour in this figure legend, the reader is referred to the web version of this article.)

4.6. Ab initio insights into reaction mechanism

As we use DFT results to obtain the principal understanding of the reaction mechanism, we neglect regioisomerism and limit our investigations to one positional isomer of each compound class. Due to approximations inherent to DFT calculations and catalyst active site modelling, difference between the reactivity of regioisomers (e.g. 2-hexene and 3-hexene) is difficult to tract with DFT. Experimental data show that this simplification is well founded. For instance, rates of hydrogenation for 2-hexanone and 3-hexanone, and for 2-hexenes and 3-hexenes, respectively, are almost indistinguishable. As shown in Fig. 8, 2-hexanone hydrodeoxygenation via 2-hexene was therefore chosen as a model reaction pathway.

The most favourable adsorption mode of 2-hexanone is $\eta_1 \mu_1$ ($E_{\text{ads}} = -119 \text{ kJ mol}^{-1}$), meaning that it binds to the sulphur-

deficient surface molybdenum atom to fill its coordination shell. Two hydrogen atoms are adsorbed on the adjacent Ni and the bridge sulphur atom. In the first highly exothermic and thus irreversible ($\Delta E = -106 \text{ kJ mol}^{-1}$) step with activation barrier of 10 kJ mol⁻¹, hydrogen atom from Ni (hydridic species) binds to carbon, yielding 2-hydroxy intermediate. In the following rate-determining step ($\Delta E = -29 \text{ kJ mol}^{-1}$) with the activation energy of 45 kJ mol⁻¹, it then attracts the acidic hydrogen from the sulphhydryl group, yielding 2-hexanol.

The ensuing 2-hexanol does not readily deoxygenate on the sulphided active site. Cleavage of the C–O bond yields OH group bound to Mo and 2-hexanyl intermediate bound to Ni. Activation energy for this step is 138 kJ mol⁻¹. Direct hydrogenolysis *via* the attacking hydridic species (H–Ni) occurs as a S_N2 reaction and needs to be considered only at high temperatures on the account of its high activation barrier of 134 kJ mol⁻¹.

Instead, the majority of 2-hexanol converts to first 2-hexanyl intermediate and subsequently *trans*-2-hexene over a vacancy active site (green pathway in Figs. 7 and 8). These both elementary steps have comparable activation energies of 64–65 kJ mol⁻¹.

Most notably, our mechanism does not postulate the formation of a thiol intermediate, which is proposed by Dupont et al. for 1-propanol hydrodeoxygenation on the same model catalyst [50]. For C–O bond cleavage in 2-hexanol resulting in 2-hexanethiol, our calculated activation energy is 160 kJ mol⁻¹. Reduction of 2-hexanethiol to hexane is also improbable with activation energy 153 kJ mol⁻¹. These barriers, while in good agreement with theoretical work of Dupont et al., are not confirmed by our experimental work. Additionally, this pathway would not take the formation of hexenes into account.

Finally, *trans*-2-hexene is hydrogenated to hexane, again over sulphided active site. In the first step with activation barrier of 30 kJ mol⁻¹, acidic hydrogen from sulphhydryl group is added to the double bond, yielding 2-hexanyl intermediate. In the second, rate-determining step with activation energy 49 kJ mol⁻¹, hexanyl is hydrogenated with hydrogen from the Ni to form hexane. The overall reaction is highly exothermic (-213 kJ mol^{-1}).

Energy profile for all three steps of HDO of 2-hexanone (*via* 2-hexanol and *trans*-2-hexane) into hexane is shown in Fig. 9.

It should be noted that reactions of hexenes isomerisation are much faster than other reactions (their formation and hydrogenation) and proceed both on a catalyst and homogenously, warranting a different approach. For microkinetic modelling purposes, relative concentrations of hexene isomers were assumed to represent

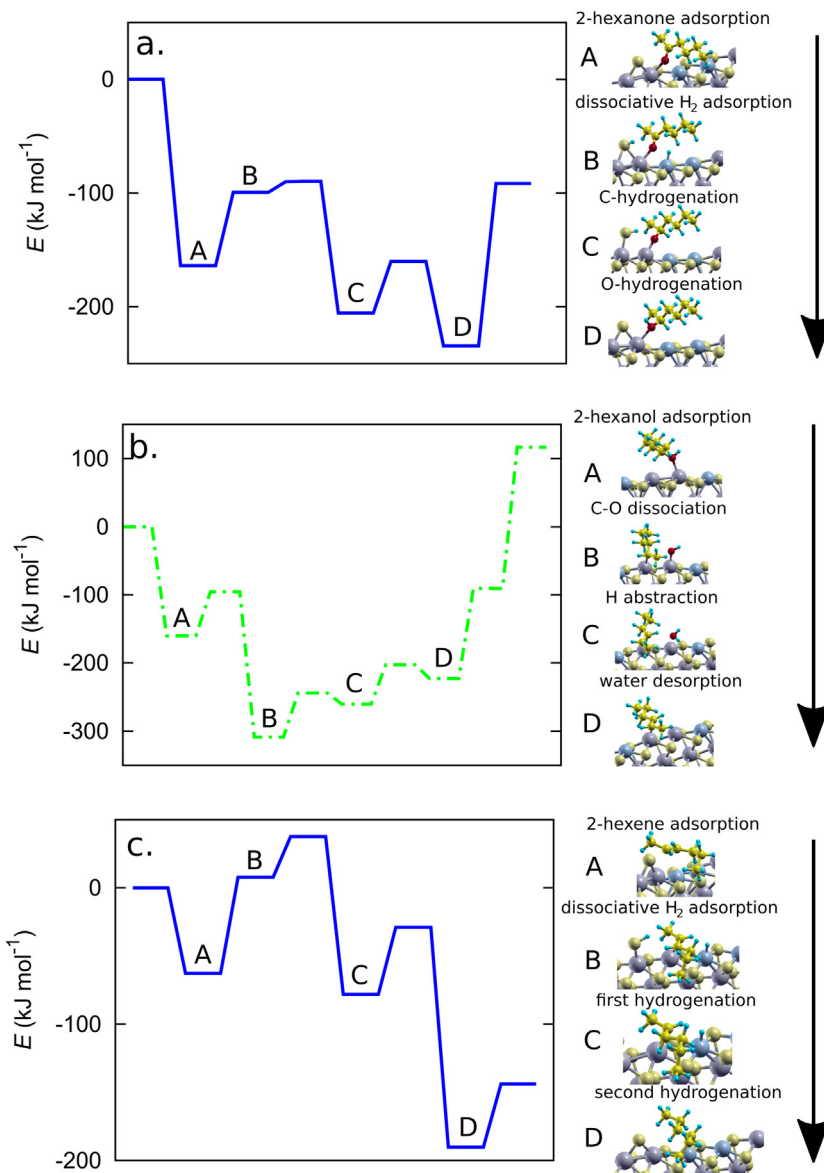


Fig. 9. Potential energy surface for HDO of a) 2-hexanone to 2-hexanol, b) 2-hexanol to *trans*-2-hexene and c) *trans*-2-hexene to hexane, all starting with desorbed reactants and finishing with desorbed products. Colour codes as in Fig. 8. Note the key in the right-hand side and description of steps linking the figures.

Table 9

Equilibrium constants for isomerisations of hexenes, obtained from first-principles DFT calculations.

Equilibrium	K_{eq} $T = 200^{\circ}\text{C}$	K_{eq} $T = 225^{\circ}\text{C}$	K_{eq} $T = 250^{\circ}\text{C}$	K_{eq} $T = 275^{\circ}\text{C}$
$1\text{-hexene} \leftrightarrow cis\text{-}2\text{-hexene}$	0.12	0.13	0.14	0.15
$1\text{-hexene} \leftrightarrow trans\text{-}2\text{-hexene}$	0.03	0.04	0.05	0.05
$cis\text{-}2\text{-hexene} \leftrightarrow trans\text{-}2\text{-hexene}$	0.28	0.31	0.33	0.35
$cis\text{-}2\text{-hexene} \leftrightarrow cis\text{-}3\text{-hexene}$	1.87	1.82	1.78	1.74
$trans\text{-}2\text{-hexene} \leftrightarrow trans\text{-}3\text{-hexene}$	1.34	1.32	1.30	1.28
$trans\text{-}3\text{-hexene} \leftrightarrow cis\text{-}3\text{-hexene}$	0.20	0.22	0.24	0.26

thermodynamic equilibria at all times. Equilibrium constants for each pair of hexenes considered (see Fig. 2 and Table 9) were obtained from density functional theory at different temperatures (see Table 9). Relative stability of the isomers was determined as *trans*-2-hexene > *trans*-3-hexene > *cis*-2-hexene > *cis*-3-hexene > 1-hexene. This is in good, but not perfect, agreement with our experimental data, where *cis*-2-hexene was more abundant than *trans*-3-hexene.

5. Conclusions

This work provides a novel insight into catalytic and non-catalytic reaction mechanism and kinetics involved in hydrodeoxygénéation of oxygen-containing functional groups located on non-terminal aliphatic carbon. Experimental results and DFT study showed that non-catalytic hydrogenation of 2-hexanone or 3-hexanone to 2-hexanol or 3-hexanol and further dehydroxylations are negligible at 250 °C and 5 MPa of H_2 . First-principles calculations confirmed that ketone hydrogenation by molecular hydrogen is an extremely improbable reaction, which requires overcoming a reaction barrier of 287 kJ mol^{-1} . This work also unravels the homogeneous double-bond shift and *cis-trans* isomerisation, both rates being greatly dependent on the H_2 partial pressure (200-fold higher at 5 MPa of H_2 than under pure N_2) as molecular H_2 participates in the intramolecular hydrogen transfer, according to the DFT results. On the other hand, NiMo/ $\gamma\text{-Al}_2\text{O}_3$ promotes rapid hydrogen transfer even in complete absence of molecular hydrogen, while the H_2 partial pressure of 5 MPa increases the isomerisation rates up to 9.5 fold. Industrial sulphided NiMo/ $\gamma\text{-Al}_2\text{O}_3$ showed very fast

hydrogenation (sulphided sites) and hydroxylation (vacancy sites) activity at investigated process conditions, while the position of the oxygen moiety (hydroxyl and carbonyl groups on C₂ or C₃ position on hexane chain) did not significantly affect the reaction pathways and kinetic rate constants or activation energies.

Acknowledgements

The authors gratefully acknowledge the financial support of the Slovenian Research Agency (ARRS) through the Research Core Funding Programme P2-0152. The authors would also like to thank Eurecat company for catalyst sulphidation by the Totsucat® process and Mr Vili Resnik for his enduring inspiration and warm support.

Appendix A. Supplementary data

Supplementary data associated with this article can be found, in the online version, at <http://dx.doi.org/10.1016/j.apcatab.2017.06.046>.

References

- [1] Y.-B. Huang, Y. Fu, Hydrolysis of cellulose to glucose by solid acid catalysts, *Green Chem.* 15 (2013) 1095–1111, <http://dx.doi.org/10.1039/C3GC40136G>.
- [2] A.M. Ruppert, K. Weinberg, R. Palkovits, Hydrogenolysis goes bio: from carbohydrates and sugar alcohols to platform chemicals, *Angew. Chem. Int. Ed.* 51 (2012) 2564–2601, <http://dx.doi.org/10.1002/anie.201105125>.
- [3] M.J. Climent, A. Corma, S. Iborra, Converting carbohydrates to bulk chemicals and fine chemicals over heterogeneous catalysts, *Green Chem.* 13 (2011) 520–540, <http://dx.doi.org/10.1039/C0GC00639D>.
- [4] S. Van de Vyver, J. Geboers, W. Schutyser, M. Dusselier, P. Eloy, E. Dornez, J.W. Seo, C.M. Courtin, E.M. Gaigneaux, P.A. Jacobs, B.F. Sels, Tuning the acid/metal balance of carbon nanofiber-supported nickel catalysts for hydrolytic hydrogenation of cellulose, *ChemSusChem* 5 (2012) 1549–1558, <http://dx.doi.org/10.1002/cssc.201100782>.
- [5] E.-M. Ryymä, M.L. Honkela, T.-R. Viljava, A.O.I. Krause, Insight to sulfur species in the hydrodeoxygénéation of aliphatic esters over sulfided NiMo/γ-Al₂O₃ catalyst, *Appl. Catal. A Gen.* 358 (2009) 42–48, <http://dx.doi.org/10.1016/j.apcata.2009.01.035>.
- [6] A.M. Robinson, J.E. Hensley, J.W. Medlin, Bifunctional catalysts for upgrading of biomass-Derived oxygenates: a review, *ACS Catal.* (2016) 5026–5043, <http://dx.doi.org/10.1021/acscatal.6b00923>.
- [7] A. Corma, S. Iborra, A. Velty, Chemical routes for the transformation of biomass into chemicals, *Chem. Rev.* 107 (2007) 2411–2502, <http://dx.doi.org/10.1021/cr050989d>.
- [8] E. Furimsky, Catalytic hydrodeoxygénéation, *Appl. Catal. A Gen.* 199 (2000) 147–190, [http://dx.doi.org/10.1016/S0926-860X\(99\)00555-4](http://dx.doi.org/10.1016/S0926-860X(99)00555-4).
- [9] R.V. Chaudhari, A. Torres, X. Jin, B. Subramaniam, Multiphase catalytic hydrogenolysis/hydrodeoxygénéation processes for chemicals from renewable feedstocks: kinetics, mechanism, and reaction engineering, *Ind. Eng. Chem. Res.* 52 (2013) 15226–15243, <http://dx.doi.org/10.1021/ie400709d>.
- [10] J.N. Chhedra, J.A. Dumesic, An overview of dehydration, aldol-condensation and hydrogenation processes for production of liquid alkanes from biomass-derived carbohydrates, *Catal. Today* 123 (2007) 59–70, <http://dx.doi.org/10.1016/j.cattod.2006.12.006>.
- [11] M.A. Alotaibi, E.F. Kozhevnikova, I.V. Kozhevnikov, Efficient hydrodeoxygénéation of biomass-derived ketones over bifunctional Pt-polyoxometalate catalyst, *Chem. Commun.* 48 (2012) 7194–7196, <http://dx.doi.org/10.1039/C2CC33189F>.
- [12] L. Vilcög, A. Cabiac, C. Especel, S. Lacombe, D. Duprez, New insights into the mechanism of sorbitol transformation over an original bifunctional catalytic system, *J. Catal.* 320 (2014) 16–25, <http://dx.doi.org/10.1016/j.jcat.2014.09.012>.
- [13] B. Peng, C. Zhao, I. Mejía-Centeno, G.A. Fuentes, A. Jentys, J.A. Lercher, Comparison of kinetics and reaction pathways for hydrodeoxygénéation of C3 alcohols on Pt/Al₂O₃, *Catal. Today* 183 (2012) 3–9, <http://dx.doi.org/10.1016/j.cattod.2011.10.022>.
- [14] O. Weisser, S. Landa, Sulphide Catalysts: Their Properties and Applications, Pergamon Press, 1973, 2017 <https://books.google.si/books?id=iSLwAAAAMAAJ>.
- [15] O.I. Senol, E.M. Ryymä, T.R. Viljava, A.O.I. Krause, Effect of hydrogen sulphide on the hydrodeoxygénéation of aromatic and aliphatic oxygenates on sulphided catalysts, *J. Mol. Catal. a-Chem.* 277 (2007) 107–112, <http://dx.doi.org/10.1016/j.molcata.2007.07.033>.
- [16] O.I. Senol, T.R. Viljava, A.O.I. Krause, Hydrodeoxygénéation of aliphatic esters on sulphided NiMo/γ-Al₂O₃ and CoMo/γ-Al₂O₃ catalyst: the effect of water, *Catal. Today* 106 (2005) 186–189, <http://dx.doi.org/10.1016/j.cattod.2005.07.129>.
- [17] Z. He, X. Wang, Hydrodeoxygénéation of model compounds and catalytic systems for pyrolysis bio-oils upgrading, *Catal. Sustain. Energy* 1 (28) (2012), <http://dx.doi.org/10.2478/cse-2012-0004>.
- [18] P.L. Mills, R.V. Chaudhari, Multiphase catalytic reactor engineering and design for pharmaceuticals and fine chemicals, *Catal. Today* 37 (1997) 367–404, [http://dx.doi.org/10.1016/S0920-5861\(97\)00028-X](http://dx.doi.org/10.1016/S0920-5861(97)00028-X).
- [19] G. Biardi, G. Baldi, Three-phase catalytic reactors, *Catal. Today* 52 (1999) 223–234, [http://dx.doi.org/10.1016/S0920-5861\(99\)00077-2](http://dx.doi.org/10.1016/S0920-5861(99)00077-2).
- [20] N. Guo, S. Caratzoulas, D.J. Doren, S.I. Sandler, D.G. Vlachos, A perspective on the modeling of biomass processing, *Energy Environ. Sci.* 5 (2012) 6703–6716, <http://dx.doi.org/10.1039/C2EE02663E>.
- [21] M.I. Fadlalla, H.B. Friedrich, The effect of the oxidation environment on the activity and selectivity to aromatics and octenes over cobalt molybdate in the oxidative dehydrogenation of n-octane, *Catal. Sci. Technol.* 4 (2014) 4378–4385, <http://dx.doi.org/10.1039/C4CY00812J>.
- [22] M. Grilc, B. Likozar, J. Levec, Hydrodeoxygénéation and hydrocracking of solvolysed lignocellulosic biomass by oxide, reduced and sulphide form of NiMo, Ni, Mo and Pd catalysts, *Appl. Catal. B Environ.* 150–151 (2014) 275–287, <http://dx.doi.org/10.1016/j.apcatab.2013.12.030>.
- [23] M. Grilc, B. Likozar, J. Levec, Simultaneous liquefaction and hydrodeoxygénéation of lignocellulosic biomass over NiMo/Al₂O₃, Pd/Al₂O₃, and zeolite Y catalysts in hydrogen donor solvents, *ChemCatChem* 8 (2016) 180–191, <http://dx.doi.org/10.1002/cctc.201500840>.
- [24] T.Y. Kwak, G.A. Mansoori, Van der waals mixing rules for cubic equations of state. Applications for supercritical fluid extraction modelling, *Chem. Eng. Sci.* 41 (1986) 1303–1309, [http://dx.doi.org/10.1016/0009-2509\(86\)87103-2](http://dx.doi.org/10.1016/0009-2509(86)87103-2).
- [25] W. Gao, R.L. Robinson, K.A.M. Gasem, High-Pressure solubilities of hydrogen, nitrogen, and carbon monoxide in dodecane from 344 to 410 K at pressures to 13.2 MPa, *J. Chem. Eng. Data* 44 (1999) 130–132, <http://dx.doi.org/10.1021/je9801664>.
- [26] G. Froment, K.B. Bischoff, J. De Wilde, Chemical Reactor Analysis and Design, 3rd edition, John Wiley & Sons, Incorporated, 2010, 2017 <https://books.google.si/books?id=lbQbAAAQBAJ>.
- [27] I.Rolo Lara, I.Caco Ana, J.Queimada António, M.Marrucho Isabel, Surface tension of heptane, decane, hexadecane, eicosane, and some of their binary mixtures, *J. Chem. Eng. Data* 47 (2002) 1442–1445, <http://dx.doi.org/10.1021/je025536+>.
- [28] R.C. Reid, J.M. Prausnitz, B.E. Poling, *The Properties of Gases and Liquids*, McGraw-Hill, New York, 1987.
- [29] M.A. Matthews, J.B. Rodden, A. Akgerman, High-temperature diffusion of hydrogen, carbon monoxide, and carbon dioxide in liquid n-heptane, n-dodecane, and n-hexadecane, *J. Chem. Eng. Data* 32 (1987) 319–322, <http://dx.doi.org/10.1021/je00049a012>.
- [30] C.N. Satterfield, *The Role of Diffusion in Catalysis*, Addison-Wesley Pub. Co., 1963.
- [31] E.W. Lemmon, M.L. Huber, Thermodynamic properties of n-dodecane, *Energy Fuels* 18 (2004) 960–967, <http://dx.doi.org/10.1021/ef0341062>.
- [32] G. Paolo, B. Stefano, B. Nicola, C. Matteo, C. Roberto, C. Carlo, C. Davide, L.C. Guido, C. Matteo, D. Ismaila, C. Andrea Dal, G. Stefano de, F. Stefano, F. Guido, G. Ralph, G. Uwe, G. Christos, K. Anton, L. Michele, M.-S. Layla, M. Nicola, M. Francesco, M. Riccardo, P. Stefano, P. Alfredo, P. Lorenzo, S. Carlo, S. Sandro, S. Gabriele, P.S. Ari, S. Alexander, U. Paolo, M.W. Renata, QUANTUM ESPRESSO: a modular and open-source software project for quantum simulations of materials, *J. Phys. Condens. Matter.* 21 (2009) 395502 <http://stacks.iop.org/0953-8984/21/i=39/a=395502>.
- [33] J.P. Perdew, K. Burke, M. Ernzerhof, Generalized gradient approximation made simple, *Phys. Rev. Lett.* 77 (1996) 3865–3868, <http://dx.doi.org/10.1103/PhysRevLett.77.3865>.
- [34] S. Grimme, Semiempirical GGA-type density functional constructed with a long-range dispersion correction, *J. Comput. Chem.* 27 (2006) 1787–1799, <http://dx.doi.org/10.1002/jcc.20495>.
- [35] V. Barone, M. Casarin, D. Forrer, M. Pavone, M. Sambi, A. Vittadini, Role and effective treatment of dispersive forces in materials: polyethylene and graphite crystals as test cases, *J. Comput. Chem.* 30 (2009) 934–939, <http://dx.doi.org/10.1002/jcc.21112>.
- [36] M.J. Frisch, G.W. Trucks, H.B. Schlegel, G.E. Scuseria, M.A. Robb, J.R. Cheeseman, G. Scalmani, V. Barone, B. Mennucci, G.A. Petersson, H. Nakatsuji, M. Caricato, X. Li, H.P. Hratchian, A.F. Izmaylov, J. Bloino, G. Zheng, J.L. Sonnenberg, M. Hada, M. Ehara, K. Toyota, R. Fukuda, J. Hasegawa, M. Ishida, T. Nakajima, Y. Honda, O. Kitao, H. Nakai, T. Vreven, A. Montgomery Jr., J.E. Peralta, F. Ogliaro, M.J. Bearpark, J. Heyd, E.N. Brothers, K.N. Kudin, R. Staroverov, J. Normand, K. Ragahavachari, A.P. Rendell, J.C. Burant, S.S. Iyengar, J. Tomasi, M. Cossi, N. Rega, N.J. Millam, M. Klene, J.E. Knox, J.B. Cross, V. Bakken, C. Adamo, J. Jaramillo, R. Gomperts, R.E. Stratmann, O. Yazyev, A.J. Austin, R. Cammi, C. Pomelli, J.W. Ochterski, R.L. Martin, K. Morokuma, V.G. Zakrzewski, G.A. Voth, P. Salvador, J.J. Dannenberg, S. Dapprich, A.D. Daniels, Ö. Farkas, J.B. Foresman, J.V. Ortiz, J. Cioslowski, D.J. Fox, Gaussian 09 (2009).
- [37] D.A. McQuarrie, *Statistical Mechanics* University Science Books, 2000 <https://books.google.si/books?id=itcpPnDnjM0C>.
- [38] M. Ruinart de Brimont, C. Dupont, A. Daudin, C. Geantet, P. Raybaud, Deoxygenation mechanisms on Ni-promoted MoS₂ bulk catalysts: a combined experimental and theoretical study, *J. Catal.* 286 (2012) 153–164, <http://dx.doi.org/10.1016/j.jcat.2011.10.022>.
- [39] B. Baubert, M. Girleanu, A.-S. Gay, A.-L. Taleb, M. Moreaud, F. Wahl, V. Delattre, E. Devers, A. Hugon, O. Ersen, P. Afanasiev, P. Raybaud, Quantitative two-dimensional (2D) morphology-selectivity relationship of CoMoS

nanolayers: a combined high-Resolution high-angle annular dark field scanning transmission electron microscopy (HR HAADF-STEM) and density functional theory (DFT) study, *ACS Catal.* 6 (2016) 1081–1092, <http://dx.doi.org/10.1021/acscatal.5b02628>.

[40] P. Raybaud, J. Hafner, G. Kresse, S. Kasztelan, H. Toulhoat, Ab initio study of the H₂-H₂S/MoS₂ gas-Solid interface: the nature of the catalytically active sites, *J. Catal.* 189 (2000) 129–146, <http://dx.doi.org/10.1006/jcat.1999.2698>.

[41] J.F. Harrod, A.J. Chalk, Homogeneous catalysis. I. Double bond migration in n-olefins, catalyzed by group VIII metal complexes, *J. Am. Chem. Soc.* 86 (1964) 1776–1779, <http://dx.doi.org/10.1021/ja01063a024>.

[42] R. Durand, P. Geneste, C. Moreau, J.L. Pirat, Heterogeneous hydrodeoxygenation of ketones and alcohols on sulfided NiO-MoO₃-γ-Al₂O₃ catalyst, *J. Catal.* 90 (1984) 147–149, [http://dx.doi.org/10.1016/0021-9517\(84\)90095-2](http://dx.doi.org/10.1016/0021-9517(84)90095-2).

[43] V. Chandra Sekhar Palla, D. Shee, S.K. Maity, Kinetics of hydrodeoxygenation of octanol over supported nickel catalysts: a mechanistic study, *RSC Adv.* 4 (2014) 41612–41621, <http://dx.doi.org/10.1039/C4RA06826B>.

[44] O. Poole, K. Alharbi, D. Belic, E.F. Kozhevnikova, I.V. Kozhevnikov, Hydrodeoxygenation of 3-pentanone over bifunctional Pt-heteropoly acid catalyst in the gas phase: enhancing effect of gold, *Appl. Catal. B Environ.* 202 (2017) 446–453, <http://dx.doi.org/10.1016/j.apcatb.2016.09.044>.

[45] A.E. King, T.J. Brooks, Y.-H. Tian, E.R. Batista, A.D. Sutton, Understanding ketone hydrodeoxygenation for the production of fuels and feedstocks from biomass, *ACS Catal.* 5 (2015) 1223–1226, <http://dx.doi.org/10.1021/cs501965w>.

[46] A. Maldonado, F. Rosas, J.R. Mora, Y. Brusco, T.C. Córdova-Sintjago, G. Chuchani, Homogeneous catalysis on the gas-phase dehydration reaction of tertiary alcohols by hydrogen bromide. Density functional theory calculation, *Mol. Phys.* 113 (2015) 282–293, <http://dx.doi.org/10.1080/00268976.2014.938707>.

[47] B. Dennis, R.G. Egeberg, P. Blom, K.G. Knudsen, Hydroprocessing of bio-oils and oxygenates to hydrocarbons. Understanding the reaction routes, *Top. Catal.* 52 (2009) 229–240, <http://dx.doi.org/10.1007/s11244-008-9159-z>.

[48] D.-Y. Peng, D.B. Robinson, A new two-constant equation of state, *Ind. Eng. Chem. Fundam.* 15 (1976) 59–64, <http://dx.doi.org/10.1021/i160057a011>.

[49] O.I. Şenol, T.R. Viljava, A.O.I. Krause, Effect of sulphiding agents on the hydrodeoxygenation of aliphatic esters on sulphided catalysts, *Appl. Catal. A Gen.* 326 (2007) 236–244, <http://dx.doi.org/10.1016/j.apcata.2007.04.022>.

[50] C. Dupont, R. Lemeur, A. Daudin, P. Raybaud, Hydrodeoxygenation pathways catalyzed by MoS₂ and NiMoS active phases: a DFT study, *J. Catal.* 279 (2011) 276–286, <http://dx.doi.org/10.1016/j.jcat.2011.01.025>.